Title

Low-Dose Exposure of WS2 Nanosheets Induces Differential Apoptosis in Lung Epithelial Cells

Journal

Environmental Science and Technology, 57(39)

ISSN

0013-936X

Authors

Coreas, Roxana
Li, Zongbo
Chen, Junyi
et al.

Publication Date

2023-10-03

DOI

10.1021/acs.est.3c01843

Low Dose Exposure of WS_2 Nanosheets Induces Differential Apoptosis in Lung Epithelial Cells

*Roxana Coreas[1], Zongbo Li[2], Junyi Chen[1], Wenwan Zhong[1,2]**

[1]Environmental Toxicology Graduate Program; [2]Department of Chemistry, University of California-Riverside, Riverside, CA 92521, USA

* Corresponding author

Prof. Wenwan Zhong, email: wenwan.zhong@ucr.edu

TOC

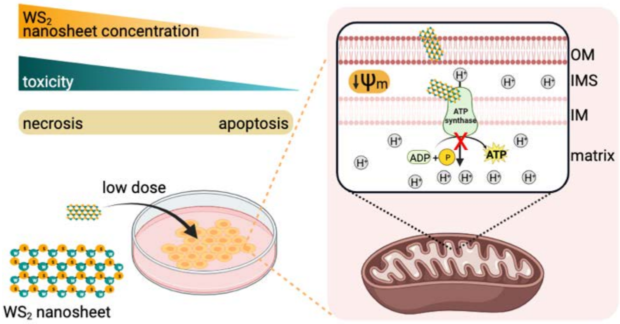
WS_2 nanosheet concentration
toxicity
necrosis
apoptosis
low dose
WS_2 nanosheet
$\downarrow\Psi_m$
OM
IMS
IM
matrix
H^+
ATP synthase
ADP + P
ATP

ABSTRACT

Escalating production and application of tungsten disulfide (WS_2) nanosheets inevitably increase environmental human exposure and warrant the necessity of studies to elucidate their biological impacts. Herein, we assessed the toxicity of WS_2 nanosheets and focused on the impacts of low doses (≤ 10 μg/mL) on normal (BEAS-2B) and tumorigenic (A549) lung epithelial cells. The low doses, which approximate real-world exposures, were found to induce cell apoptosis, while doses ≥ 50 μg/mL cause necrosis. Focused study on low-dose exposure to WS_2 nanosheets revealed more details of the impacts on both cell lines, including reduction of cell metabolic activity, induction of lipid peroxidation in cell membranes, and uncoupling of mitochondria oxidative phosphorylation that led to loss of ATP production. These phenomena, along with the expression situations of a few key proteins involved in apoptosis, point towards the occurrence of mitochondria-dependent apoptotic signaling in exposed cells. Substantial differences in responses to WS_2 exposure between normal and tumorigenic lung epithelial cells were noticed as well; specifically, BEAS-2B cells experienced more adverse effects and took up more nanosheets than A549 cells. Our results highlight the importance of dose and cell model selection in assessment of nanotoxicity. By using doses consistent with real-world exposures and comparing normal and diseased cells, we can gain knowledge to guide the development of safety precautions for mitigating the adverse impacts of nanomaterial exposure on human health.

KEYWORDS

tungsten disulfide nanosheets, mitochondria damage, apoptosis, uptake, exposure dose

SYNOPSIS

Low-dose WS_2 nanosheet exposure has severe adverse effects on normal human airway epithelial cells relative to a tumorigenic counterpart, raising human health impact concerns.

INTRODUCTION

Tungsten disulfide (WS_2) nanosheets are two-dimensional (2D) transmission metal dichalcogenides that possess high specific surface areas and unique physicochemical properties compared to their bulk counterparts[1–3]. Their use is becoming more prevalent in electronics[4,5], automotive[6,7], agricultural[8,9], and biomedical applications[10–12], and is expected to increase alongside intentional and accidental (occupational or environmental) exposures[13,14].

There have been several studies aimed at identifying the potential cytotoxicity of WS_2 nanosheets[15–19]. However, the findings have not been consistent about the dose range needed to induce toxicity even in the same types of cells[15–17], and few have examined potential programmed cell death (PCD) mechanisms[18,19]. While differences in the observed toxicity of WS_2 nanosheets could be due to variations in exposure doses, cell models, nanosheet preparation prior to cell exposure, and nanosheets' physiochemical properties (e.g. sheet thickness and surface chemistries)[20,21], more assessments of the biological impacts and studies of the toxicity induction mechanisms are required using doses consistent with real-world exposures.

The current OSHA permissible exposure limit (PEL) for insoluble tungsten is 5 mg/m^3 as a time weighted average concentration over an 8 h work period[22]. Based on dose metric calculations of nanoparticle surface-area lung burden used at NIOSH[23,24], such an PEL exposure could lead to a lung burden similar to a bolus exposure of 5 mg/kg in mice[25]. However, for the insoluble tungsten in the form of 2D WS_2 nanosheets, it is not an easy task to extrapolate *in vitro* doses from bolus exposures[26,27]. In their study of pulmonary toxicity of metal oxide nanoparticles, Cai *et al.* extrapolated that the bolus exposure of 1–12 mg/kg of metal oxides in mice was approximately equivalent to exposing cells to 1.6–16 μg/mL metal oxides, assuming homogeneous distribution of the nanomaterials in cell culture media, the alveolar epithelium surface area of 0.05

m^2, a mouse body weight of 25 g, and metal oxide settlement higher than 70%[25]. Certainly the physicochemical properties of the material, sedimentation during cell incubation, and many other factors should be considered to attain precise dosimetry estimation[28]. Still, using the same assumptions, we estimated the bolus exposure limit of 5 mg/kg for the insoluble tungsten could be similar to exposing a cell layer to a homogenized solution of WS_2 (~ 74% (mass percentage) of W in WS_2) nanosheets at a concentration well below 10 µg/mL.

Herein, we exposed normal and tumorigenic human lung epithelial cells (BEAS-2B and A549, correspondingly) to WS_2 nanosheets and studied the cellular impacts induced by the nanosheets at biologically relevant concentrations (1 – 10 µg/mL). Cell uptake, metabolic function, mitochondria-based ATP production, and PCD mechanisms activated through caspase cascades were investigated, in an effort to gain some understanding on how adverse impacts were raised by WS_2.

MATERIALS AND METHODS

Endocytosis inhibitors assay. Cells were seeded and grown as mentioned in SI. Prior to WS_2 nanosheet exposure, BEAS-2B cells were exposed to 25 nM genistein, 2 µM cytochalasin D, or 25 µM chlorpromazine HCl, and A549 were exposed to 750 nM genistein, 2.5 µM cytochalasin D, or 50 µM chlorpromazine hydrochloride for 2 h. Afterwards, cells were washed 2× with 1× PBS and exposed to the various concentrations of WS_2 nanosheets for 24 h. Cellular metabolic activity was assessed with CCK-8, as described in Supplementary Information (SI).

ATP production rate with Seahorse XFp. A549 and BEAS-2B cells were seeded at 12,000 and 20,000 cells/well for 24 h pre-exposure assays and at 20,000 and 30,000 cells/well for real-time assays, respectively. For pre-exposure, cells were dosed with 0 or 10 µg/mL WS_2 for 24 h.

Both pre-exposed cells and cells used for real-time assays were washed 1× and the media was replaced with pre-warmed XF DMEM supplemented with 1 mM sodium pyruvate, 10 mM glucose and 2 mM glutamine (pH 7.4, 2.5 mmol/L/pH buffer factor). Cells were incubated in a non-CO_2 incubator at 37°C for 1 h prior to analysis. Oxygen consumption rates and extracellular acidification rates were measured with the real-time ATP rate assay (Agilent, USA). Cellular protein concentration was quantified with Qubit Broad Range (Thermo Scientific) to normalize data. Analysis was performed with the Agilent Seahorse Analytics web application.

Cellular uptake measurement with ICP-OES. Following exposure to 0, 5, or 10 µg/mL WS_2, cells were collected, washed 3 times with 1× PBS, and resuspended with 0.5 mL of 1× PBS. Mitochondria from exposed cells (10 µg/mL) were also isolated as described in SI. Intact cells and isolated mitochondria were dissolved with 8 mL of aqua regia for 24 h. The mixtures were boiled for 10 minutes until ~ 1 mL was left in the beaker and then diluted with 10 mL of ultrapure H_2O. The solutions were filtered with 0.22 µm PES filters and analyzed with a Perkin-Elmer Optima 7300DV inductively coupled plasma optical emission spectrometer. ICP-OES instrument settings during measurement and uptake calculation formula can be found in SI.

Statistics. Data analysis was conducted with Prism 9.4.1 for macOS (GraphPad Software). Asterisks within graphs represent significant p values: *: $p < 0.5$, **: $p < 0.01$, ***: $p < 0.001$, ****: $p < 0.0001$; ns: non-significant.

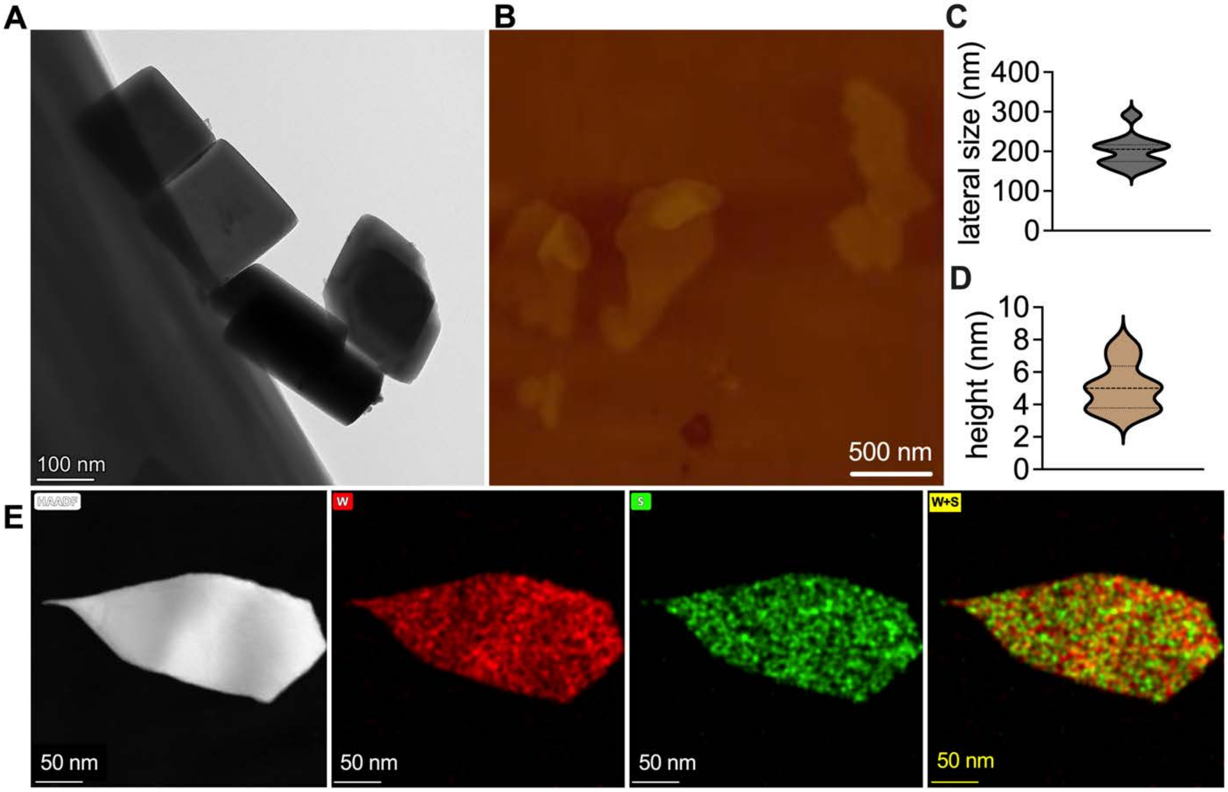

Figure 1. **Characterization of the WS_2 nanosheets.** A) TEM and B) AFM images of WS_2 nanosheets. Average C) lateral (n = 11, TEM) and D) height (n = 8, AFM) measurements are shown as violin plots in which bold dashed lines denote averages and violin widths represent measurement frequencies. E) HAADF and EDS images of a WS_2 nanosheet. W and S atoms are shown in red and green, respectively. Merged EDS images show distribution of colocalized W and S atoms (in yellow).

RESULTS

Physicochemical Characterization of WS_2 Nanosheets. The WS_2 nanosheets were synthesized and suspended in 10 mg/mL nonionic Pluronic F108 (PF108) by the Nanotechnology Health Implications Research (NHIR) consortium at the HSPH-NIEHS Nanosafety Center[19], and characterized before their use in our study. TEM images depict the sheet-like structure of the WS_2 nanosheets with an average lateral size of 200 ± 37 nm (**Figures 1A, 1C**), agreeing well with the average lateral dimensions found by NTA and DLS (**Supporting Figure S-1, S-2**). The thickness of the nanosheets measured by AFM was 5.1 ± 1.4 nm (**Figures 1B, 1D**), consistent with previous findings[19]. These measurements suggested that there was no aggregation of the nanosheets upon material transportation and storage.

EDS mapping of the distribution of tungsten (W) and sulfur (S) across the nanosheet surface (**Figure 1E**) showed the atomic fractions for S and W being 30.7 ± 7 % and 23.8 ± 4 %, respectively. The mass fractions for C and O, originating from PF108, were 4.1 ± 0.4 % and 0.6 ± 0.1 % (**Figure S-3**). The UV-Vis spectra of the WS_2 nanosheets further confirmed the chemical structure, exhibiting the exciton peak at 642 nm consistent with the optical band gap absorption of WS_2 fine particles (**Figure S-4**)[29]. FTIR spectra revealed the S-S stretching vibration band at 526 cm^{-1}; the stretching of C-H bonds at 2880 and 1465 cm^{-1}, and the stretching of C-O bonds at 1093 cm^{-1}, corroborated the adsorption of PF108 on the WS_2 surfaces (**Figure S-5**). Moreover, surface and edge S^{2-} endowed the nanosheets with a negative ζ-potential of -33.44 mV when dispersed in water (**Figure S-6**).

The negative ζ-potential helps the nanosheets well dispersed in water. Dispersion in the cell culture media (CCM) supplemented with 10% fetal bovine serum did not induce changes to WS_2 size (**Fig. S-2**) nor ζ-potential (**Fig. S-6**), ruling out the possibility of significant nanosheet aggregation occurring nor protein corona formation. We also conducted SDS-PAGE to analyze the proteins potentially adsorbed on 50 µg/mL WS_2 during 1 h incubation in the CCM and found negligible proteins on the gel (**Figure S-7**). PF108 may have adsorbed on the nanosheet surface and contributed to their low protein adsorption and high dispersity in the culture media.

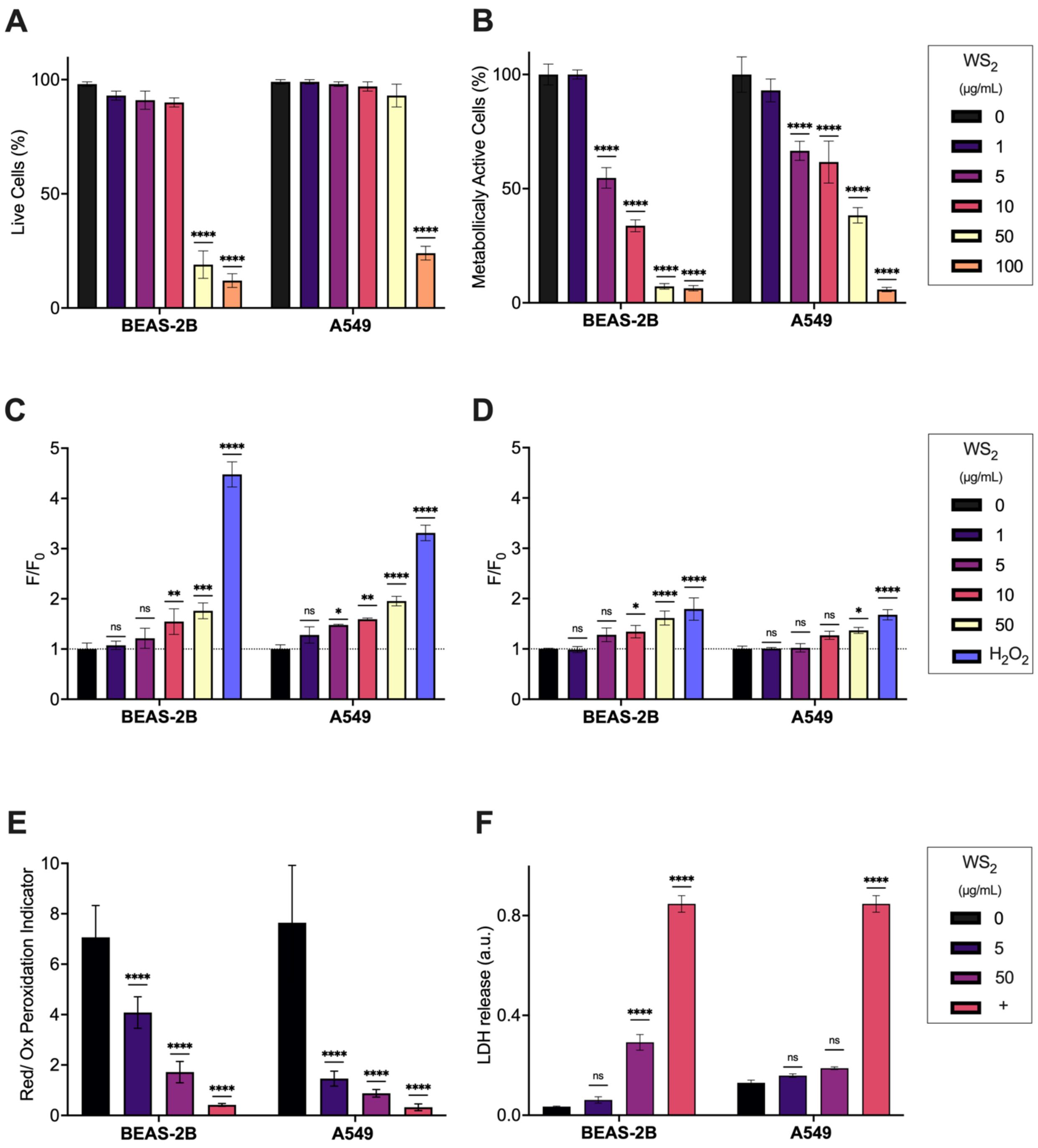

Figure 2. **Evaluation of cytotoxicity, metabolic efficiency, and oxidative stress induced by WS$_2$ exposure.** The percentage of **A)** live and **B)** metabolically active BEAS-2B and A549 cells following 24 h treatment with WS$_2$ nanosheets (n = 3). Endogenous oxidative stress measured in cells using **C)** 2× Deep Red and **D)** 5 µM CM-H$_2$DCF following 24 h exposure to WS$_2$ nanosheets (n = 3). Cells treated with 1 mM H$_2$O$_2$ (1 h) served as the positive control. **E)** Quantification of WS$_2$ induced peroxidation (n = 8) and **F)** LDH release (n = 3) in cells. The positive control in C&D was 100 µM cumene hydroperoxide (1 h) and that in E&F, depicted by +, was LDH. All

bars represent the mean ± SD; cells treated with the WS_2 nanosheets were compared with the corresponding untreated cells (0 µg/mL, black bars in all figures) with 2-way ANOVA.

WS_2 Induced Toxicity in BEAS-2B and A549. Occupational exposure to WS_2 nanosheets is presumed to occur primarily via inhalation[14,30]. Therefore, this work utilized the standard cell lines used in analysis of inhaled toxicants[31]: normal (BEAS-2B) and cancerous (A549) lung epithelial cells. Cells were exposed for 24 h to a range of concentrations (0 – 100 µg/mL) of WS_2. Trypan blue and CCK8 were used to assess live (**Figure 2A**) and metabolically active (**Fig. 2B, S-8**) cells, respectively. While a large percentage of cell death (~ 80%) was only induced at doses ≥ 50 µg/mL in BEAS-2B cells and ≥ 100 µg/mL in A549 cells, 30-40% of both cells experienced significant loss of their metabolic activity with doses ≥ 5 µg/mL, compared to untreated controls. BEAS-2B cells were more sensitive to WS_2 exposure relative to A549, with more rapid reduction in the percentage of live (**Fig. 2A**) and metabolically active (**Fig. 2B**) cells with increasing WS_2 concentrations. We also confirmed that the observed toxicity was induced by the nanosheets rather than the surfactant coating, because PF108 was non-cytotoxic at concentrations that correspond to the levels calculated in the WS_2 nanosheet suspensions used for cell assays (**Figure S-9**).

To see whether the diminishment of metabolically functional cells could be a result of elevated oxidative stress[32], we measured cellular endogenous ROS levels with Deep Red and CM-H_2DCF ROS probes. Both dyes revealed elevated ROS levels resulting from exposure to nanosheets in doses > 10 µg/mL in both cells (**Figure 2C & 2D**), but the ROS increases were in small magnitudes and could not be the main cause of the substantial cell death observed. We also ruled out the possibility of indicator oxidation due to the intrinsic surface reactivity of the WS_2 nanosheets[33], by confirming that the WS_2 nanosheets could not oxidize H_2DCF in an abiotic environment lacking H_2O_2 (**Figure S-10**).

Agreeing with the reduced metabolic activity, we observed concentration-dependent alterations to cell morphologies following a 24 h exposure to WS_2 nanosheets (**Figure S-11**). At the highest concentration used (100 µg/mL), both cells displayed cell swelling, with potential disintegration, which are signature morphology of ferroptosis and necroptosis[34] and were found to occur in cells exposed to a high dose (200 µg/mL) of WS_2 nanosheets[18]. At low-dose exposures, BEAS-2B exhibited cell shrinkage and blebbing when exposed to 5 µg/mL WS_2, with notable loss of the typical elongated structure of epithelial cells, as well as cell condensation and fragmentation observed at 10 µg/mL (**Fig. S-11**). Such alterations to cell morphology are indicative of apoptosis[35]. In contrast, these low doses only made A549 cells slightly rounded and disrupted cell-cell adhesion.

Loss of Cell Membrane Integrity Provoked by WS_2 Nanosheets. Alterations to cell morphology could result from membrane damage or remodeling during PCD[36]. Therefore, we assessed cell membrane integrity by measurements of lipid peroxidation (**Fig. 2E, S-12 & S-13**) and leakage of lactate dehydrogenase (LDH) from the cytosol into the cell culture supernatants (**Fig. 2F**). The ratios of the fluorescent signals emitted by the reduced (red)/oxidized (green) peroxidation indicator show that even the low exposure dose of 5 µg/mL could result in elevated peroxidation of cellular membranes in both cells, which increased with higher WS_2 concentrations (**Fig. 2E**). Although A549 cells experienced more lipid peroxidation, we only found significant LDH leakage that suggests membrane damage in BEAS-2B cells with exposure doses $\geq$ 10 µg/mL, but not in A549 (**Fig. 2F**).

In addition, we stained lysosomes and mitochondria of the WS_2-treated cells to determine their cellular location and integrity (**Figures S-14 & S-15**). While the location of lysosomes in cells treated with low doses of WS_2 did not differ as compared to the untreated controls, treatment with 50 µg/mL WS_2 resulted in lysosomes localized in cell culture supernatants. The lysosomal signal intensity normalized to cell counts increased in both cells when treated with 5 – 10 µg/mL WS_2 (**Figure S-16**); but with the dose increasing to 50 µg/mL, normalized lysosome signals decreased. Overall, the lysosomal signal intensity was higher in BEAS-2B cells than in A549 cells. In both cells, there were apparent alterations to mitochondria morphology as well. The once fiber-like structure of mitochondria, observed in untreated cells, becomes rounded upon exposure to WS_2 at the low doses; at the high dose, mitochondria morphology is relatively undistinguishable, indicating mitochondria structure disruption.

Uptake of WS_2 Nanosheets. Lipid peroxidation of the plasma membrane could result in pore formation within the membrane that allows for the influx of radicals and molecules[37] and (simulated) translocation of nanomaterials into cells[38]. The increase of lipid peroxidation and LDH leakage observed in **Fig. 2E and 2F** implied that the WS_2 nanosheets may have translocated into the cytosol. To confirm that, we employed ICP-OES to investigate WS_2 nanosheet internationalization. Cells were incubated with the nanosheets for 24 h at two exposure doses: 5 and 10 µg/mL, which had not yet induced significant cell death (**Fig. 2A**). About 5 – 13% of the administered dose were taken up by the cells (**Figure 3A**). The uptake percentage was higher in BEAS-2B than in A549 cells with both doses (**Fig. 3A**); but uptake dropped by more than half at the higher dose for both cells, possibly due to the extensive loss of metabolic activity (**Fig. 2B**).

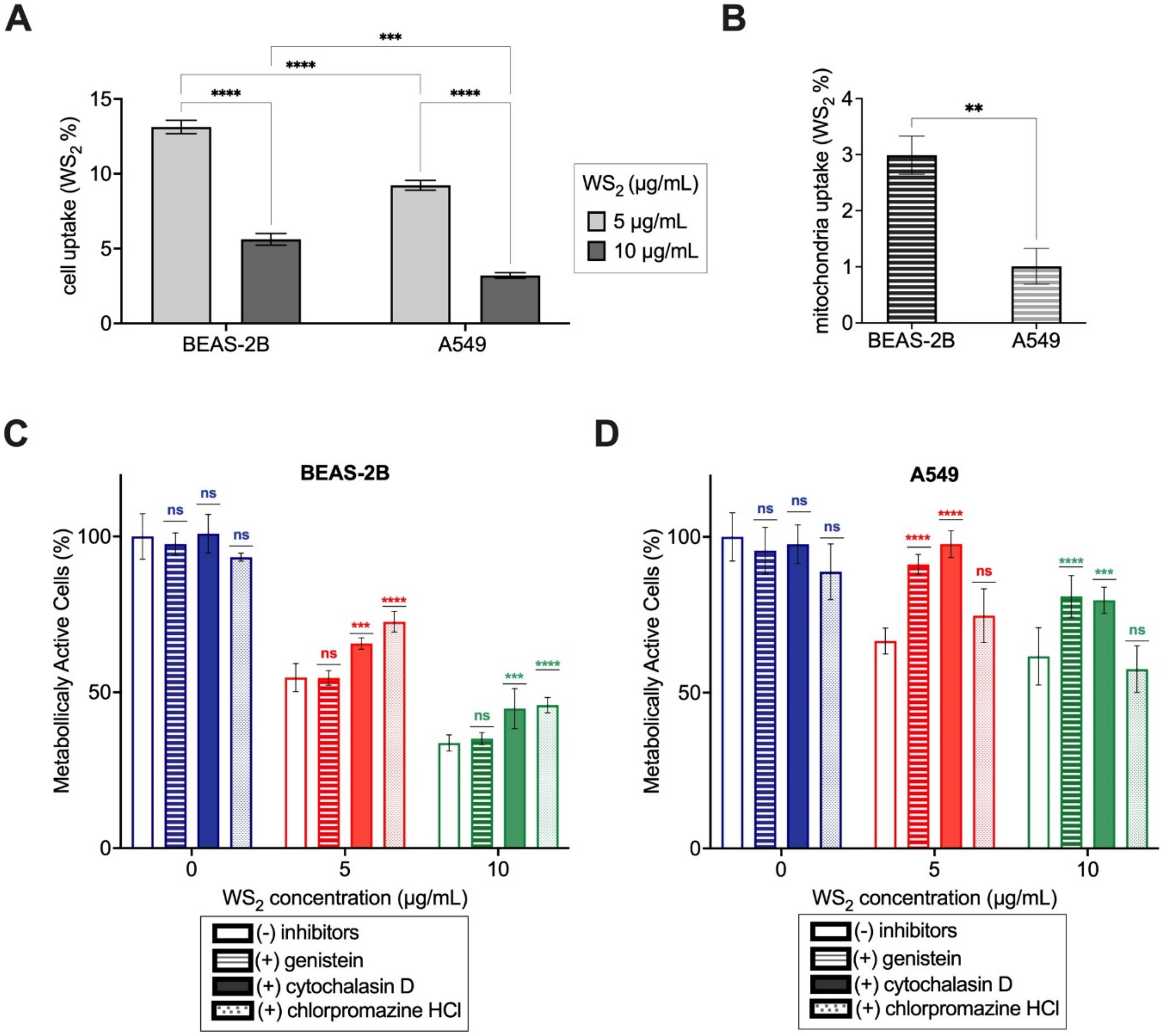

***Figure 3*. Evaluation of WS_2 uptake by cells. A)** Whole cell uptake of WS_2 nanosheets following 24 h exposure to 5 and 10 µg/mL measured with ICP-OES (n = 3). Treated cells were compared by cell type and concentration with 2-way ANOVA. **B)** Mitochondrial uptake following 24 h exposure to 10 µg/mL WS_2 assessed by ICP-OES (n = 3); mitochondrial uptake was compared between cell lines with Student's *t*-test. Evaluation of the impacts of inhibitors for different cellular uptake pathways on the metabolic activity of **C)** BEAS-2B and **D)** A549 cells induced by 24 h incubation with WS_2. Cells treated with both inhibitors and WS_2 nanosheets were compared to control cells treated only with WS_2 nanosheets (no inhibitors) at the corresponding concentrations and analyzed by 2-way ANOVA with Tukey correction. All bars represent the mean ± SD.

ICP-OES cannot discriminate between whole nanosheets and tungsten ions, and the element detected could also derive from the material strongly adsorbed to cell membranes, which were irremovable during the stringent washes. In addition, we found that ~17% of the nanosheets at 5 μg/mL were dissolved when kept in the CCM at 37 ℃ for 24 h compared to ~5% dissolution in water (**Figure S-17**). The salts and chelating ions in the CCM may have contributed to the enhanced dissolution of WS_2. To further confirm the possible uptake of intact nanosheets, we conducted TEM coupled with EDS and found nanosheets within cellular cytoplasm (**Figures S-18** & **S-19**), the shape and size of which were similar to those of the original materials (**Fig. 1C**). EDS mapping of control cells confirmed the absence of WS_2 (**Fig. S-20**).

We also investigated the potential uptake pathways, employing phagocytosis or endocytosis inhibitors: cytochalasin D, chlorpromazine HCl, and genistein. Respectively, these compounds inhibit actin-mediated phagocytosis, clathrin-mediated endocytosis, and caveolin-mediated endocytosis[39]. These inhibitors were used to pre-expose the cells for 2 h before treatment with WS_2 nanosheets. The inhibitor concentrations chosen were within the range used in previous studies of uptake pathways of nanoparticles[40–42] and maintained good cell viability during uptake experiments. We used the cell metabolic activity measured by CCK8 to reflect the level of nanosheet uptake. Our results show that cytochalasin D and chlorpromazine HCl could increase metabolic activity to some extent when BEAS-2B cells were exposed to WS_2 (**Fig. 3C**), but genistein did not show any impacts. In contrast, A549 cells responded to genistein and cytochalasin D, but not to chlorpromazine HCl (**Fig. 3D**).

Several studies have found that nanomaterial internalization can impact organelle function[43,44], and we found the metabolic activity was reduced by WS_2, therefore we further assessed the interactions of the WS_2 nanosheets with mitochondria. We isolated mitochondria from cells exposed to WS_2 nanosheets, and tested internalized tungsten levels by ICP-OES. **Figure 3B** compares the percentage of nanosheets that were found in extracted mitochondria between cell lines following an exposure to 10 μg/mL WS_2. A sizeable portion (~ 30 – 50%) of the tungsten element found in the cells was located in the mitochondria. Moreover, a higher proportion (3× more) of WS_2 was found in the mitochondria isolated from BEAS-2B than from A549.

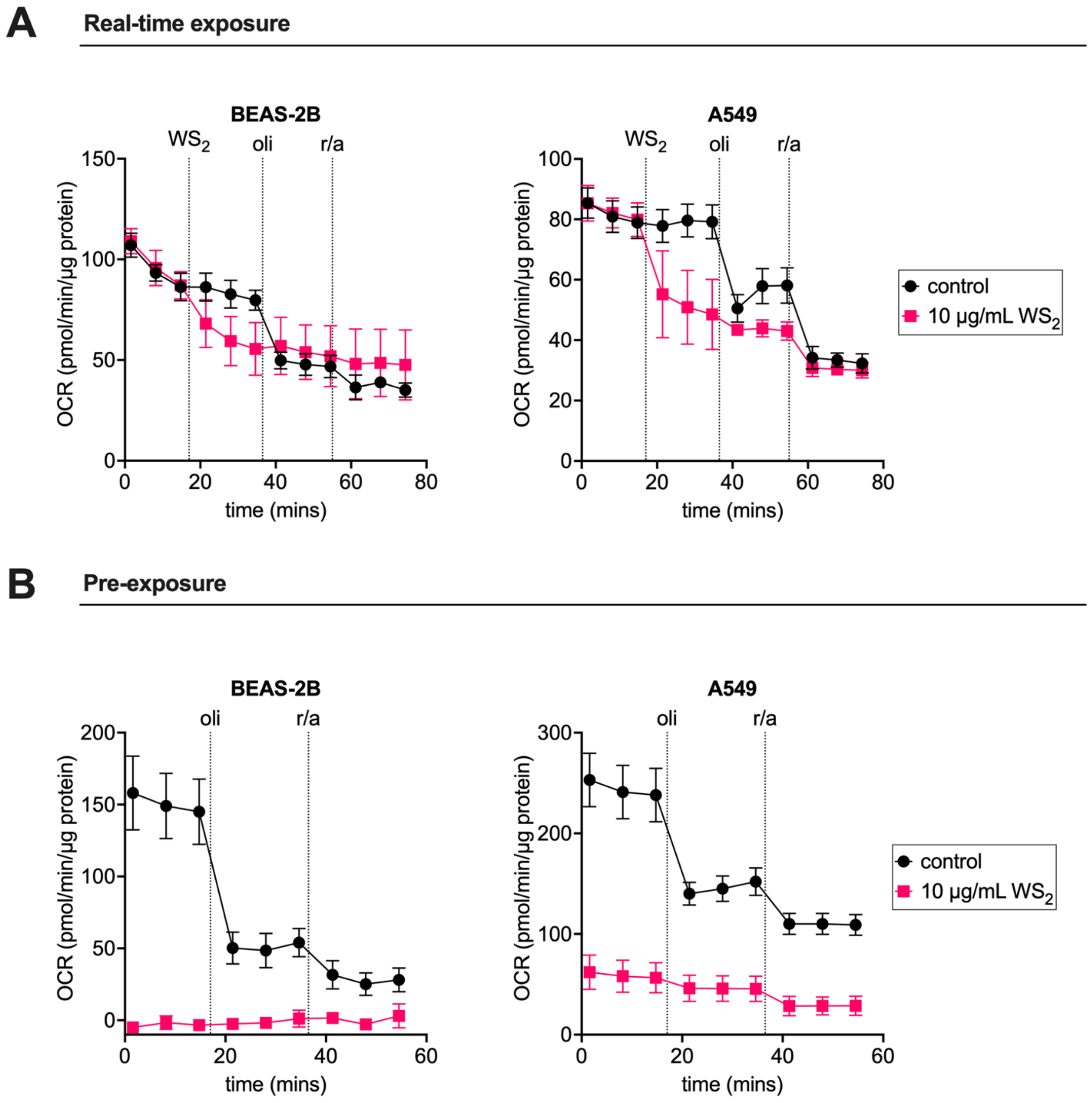

***Figure 4.* Dysregulation of mitochondria function induced by WS_2.** Oxygen consumption rates (OCR) normalized to total cellular protein of BEAS-2B and A549 cells exposed to 10 μg/mL WS_2 **A)** in real-time, and **B)** via 24 h pre-exposure prior to OCR measurement. Oligomycin (oli) and a mixture of rotenone and antimycin A (r/a) were injected at specific timepoints (to a final concentration of 1.5 μM and 0.5 μM, respectively) to assess ATP production. Each point represents an average ± SD (n = 3).

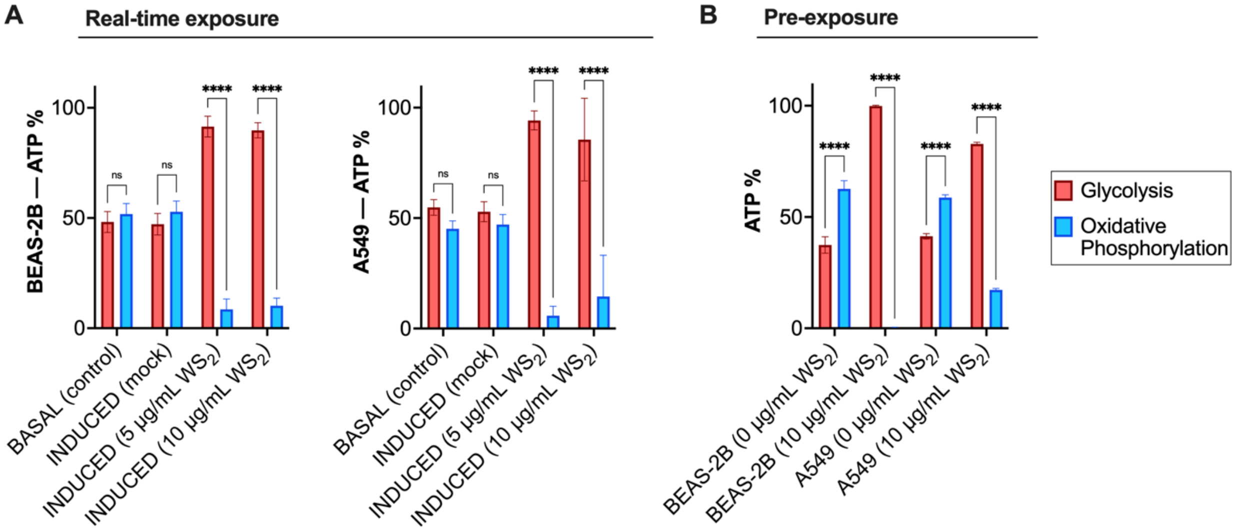

Figure 5. **WS_2 impact on ATP production. A)** The generation of ATP was calculated by measuring glycolysis and oxidative phosphorylation in BEAS-2B and A549 cells. Basal measurements were obtained from cells that were not exposed to mock (CCM) or WS_2. Induced measurements occurred in real-time as CCM (mock) or WS_2 was injected into the wells. **B)** ATP synthesis was measured in cells pre-exposed to 10 µg/mL WS_2 for 24 h. Each bar represents the average ± SD (n = 3). ATP synthesis pathways were compared with Student's *t*-test.

Dysregulation of Mitochondria Function by WS_2. The interaction with mitochondria and the reduction of cell metabolic activity prompted us to further explore impacts to the mitochondria by the nanosheets. We investigated colocalization of oxidized lipids and mitochondria, which reveals peroxidation of mitochondrial membranes and has been observed before in cells undergoing cysteine-deprivation-induced ferroptosis[45]. Indeed, colocalization was found in BEAS-2B and A549 cells (**Figures S-21** & **S-22**), with the Pearson correlation coefficients (r) of the signals from lipid peroxidation and mitochondria staining dye > 0.8. Moreover, a mitochondrial membrane potential ($\Delta\Psi_m$) indicator demonstrated substantial reductions in $\Delta\Psi_m$ in both cells (**Figure S-23**) when exposed to 10 µg/mL WS_2.

Since mitochondria, known as the powerhouse of the cell, are multifunctional regulators of cell metabolism[46], and cellular stress could lead to mitochondria damage[47], the impact of the WS_2

nanosheets on mitochondria function was further evaluated using the Seahorse Analyzer. This instrument measures cellular oxygen consumption rates (OCR) while the cells are treated with oligomycin (oli) and subsequently a mixture of rotenone/antimycin A (r/a), with the former chemical inhibiting mitochondrial ATP production by blocking ATP synthase[48]. This method has been used to evaluate the impact of nanomaterials on mitochondria functionality following nanomaterial pre-exposures[44,49]; we also recently employed this technique to assess the impacts of reduced graphene oxide on mitochondria in real-time[50]. Both modes of pre-incubation and real-time exposure were employed in this work. We found that in both cell lines, relative to the control cells (cells not exposed to nanosheets, curve in black), real-time exposure to 5 and 10 µg/mL WS_2 nanosheets (curve in magenta) significantly diminished the OCR (**Figure 4A** and **Figure S-25A**) and increased the oxygen tension (**Figure S-24 and S-25**). The inhibition of mitochondria respiratory function was also confirmed by 24 h pre-treatment of the cells with 10 µg/mL WS_2, which largely reduced OCR in both cells (**Figure 4B**). In both cases, more OCR reduction was observed in BEAS-2B cells. Agreeing with OCR measurements, both real-time exposure to WS_2 and pre-treatment with WS_2 significantly plummeted production of ATP by mitochondria and correspondingly increased the dependence of glycolysis for ATP synthesis (**Figure 5**). In BEAS-2B cells, 24 h pre-treatment with WS_2 even completely knocked out mitochondria-dependent ATP production, agreeing with the close to zero OCR observed in **Fig. 4B**.

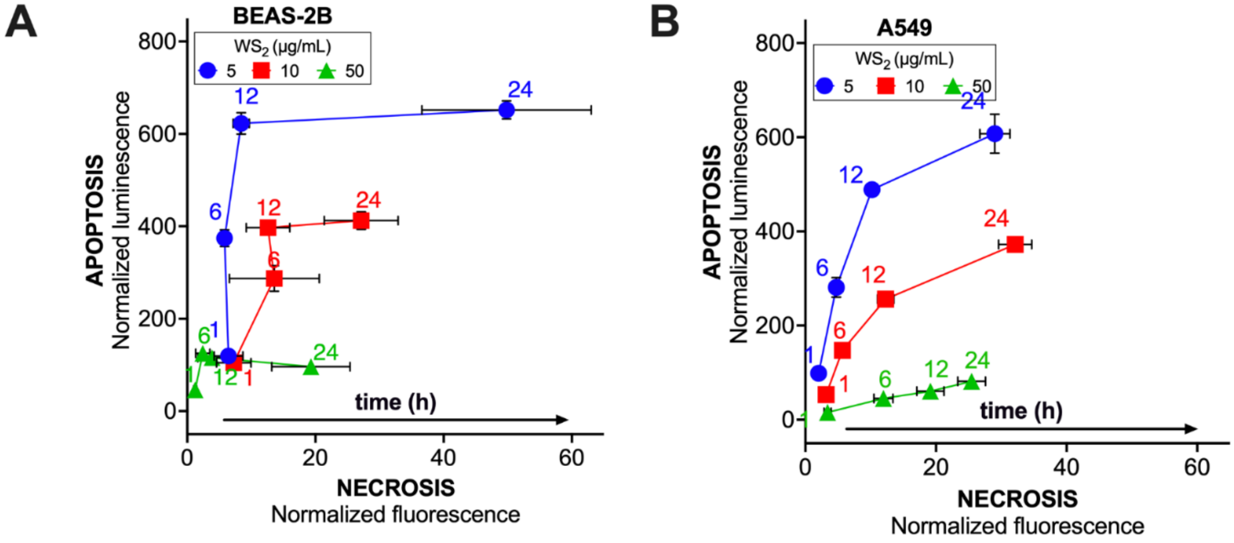

Figure 6. **Assessment of potential WS_2-induced PCD pathways.** The kinetic activation of apoptosis and necrosis by WS_2 nanosheets in **A)** BEAS-2B and **B**) A549 measured with luminescence and fluorescence, respectively (n = 3 for each assay). Each time point represents the average ± SD in both axes. Each measurement was normalized to background signals.

Apoptosis Induced by Low-Doses of WS_2. The above results revealed that low dose exposure to WS_2 can cause damage to mitochondria, which could induce apoptosis[51]. On the other hand, a previous study[18] found exposure to a high dose of 200 μg/mL WS_2 nanosheets induced ferroptosis, a special type of programmed necrosis[34]. Therefore, we employed the real-time apoptosis and necrosis assay to survey the cells following time-dependent (0 – 24 h) exposures to WS_2. The annexin V luciferase fusion proteins and a DNA-binding fluorescent dye were used to indicate if cells underwent apoptosis or necrosis[52]. As shown in **Figure 6**, exposure to 5 μg/mL of the nanosheets for up to 12 h induced an extensive luminescence but minimal fluorescence in both cell lines compared to untreated cells suggesting apoptosis as the dominant PCD mechanism. The fluorescence resulting from necrosis became significant only with 24 h treatment using this lowest exposure dose, while intensive signals indicative of both apoptosis and necrosis were observed with 10 µg/mL nanosheets. In contrast, the highest dose (50 µg/mL) elicited only fluorescence but not luminescence, indicating the triggering of necrosis by the nanosheets, agreeing with the previous report[18].

Potential mitochondria-mediated activation of apoptosis, i.e. intrinsic apoptosis, could result in cytochrome-*c* release, caspase-9 activation, and subsequent activation of caspase-3[53]. We used western blotting (WB) to analyze expression of the aforementioned proteins in cells exposed to 10 µg/mL WS_2 for different durations (**Figure S-26A&C**). Band intensities for the kinetic expression of the proteins were normalized to the loading control (GAPDH). The ratios of activated caspase proteins to inactivated pro-caspases were calculated and are shown in **Fig. S-26B&D**. We found that within the first 4 h, exposure to 10 µg/mL WS_2 activated caspase-9 and -3 in both BEAS-2B and A549 cells. However, extending the exposure duration beyond 12 h reversed this trend in BEAS-2B cells, but maintained consistent activation in A549 cells. Such a difference could be attributed to the significant decline in normal cellular functionality in BEAS-2B cells at the dose of 10 µg/mL, which affected the metabolic activities of A549 cells to a lesser degree (**Fig. 2A&B**). Meanwhile, cytochrome-*c* content in the cytosol reached peak value within a 1 h exposure and then decreased with longer exposure times in both cell lines.

Caspase-8 activation was explored in both cell lines as well because of its role in promoting the activation of caspase-3 via extrinsic apoptosis[54]. Its activation was not evident in BEAS-2B cells (**Fig. S-26**). In A549 cells, expression of caspase-8 was observed at 0 h, agreeing with previous reports that found both pro-caspase-8 and caspase-8 overexpressed in this cell line[55]. But the ratio dropped with increasing exposure time (**Fig. S-26**).

DISCUSSION

Our study revealed the strong dependence of biological impacts to cells on the exposure dosage of WS_2 nanosheets. High-dose exposures (≥ 50 µg/mL) could cause cell death (**Fig. 2**), extensive cell morphology alteration (**Fig. S-11**), mitochondrial structure disruption (**Fig. S-14&15)**, lysosome localization in the extracellular space (**Fig. S-14&15**), as well as membrane lipid peroxidation and damage (**Fig. 2E&F**). We found the PCD mechanism at this dose likely be necrosis (**Fig. 6**), as reported previously[18]. In contrast, low concentrations (5 and 10 µg/mL) of WS_2 induced substantial changes to normal metabolic activity with slight increase of ROS levels, and elevated lipid peroxidation, but not significant cell death nor LDH release (**Fig. 2**). However, nanosheet uptake to the intracellular space and even to mitochondria (**Fig. 3**), and complete disruption of mitochondria-based ATP synthesis (**Fig. 5**) were detected with these low exposure doses. The dominant PCD mechanism was determined to be apoptosis (**Fig. 6**), and in particular, intrinsic apoptosis[53], as supported by damage to mitochondria (**Fig. 4&5**) and the release of cytochrome-*c* to the cytosol, and activation of caspase-9 and -3 (**Fig. S26**).

Our work also disclosed significant differences between the two cell lines while exposed to low-dose WS_2. Firstly, BEAS-2B took up more WS_2 than A549 (**Fig. 3A**), possibly as both the intact nanosheets (**Fig. S18-20**) and the dissolved elemental forms (**Fig. S17**); and exhibited more appreciable association of the nanosheets with mitochondria (**Fig. 3B**). The uptake should not be the result of extensive membrane damage which was not observed at these low doses (**Fig. 2E and 2F**); and dropped in both cells when treated with a dose (10 µg/mL) that significantly reduced metabolic activity (**Fig. 2B**), hinting active uptake. Indeed, actin-mediated phagocytosis was identified as one of the uptake mechanisms in both cell lines. BEAS-2B also took up the nanosheets via clathrin-mediated endocytosis while A549 through a caveolin-dependent pathway (**Fig.**

3C&D). However, none of the uptake pathway inhibitors were able to completely block the nanosheet-induced cytotoxicity suggesting other unrevealed contributors to WS_2 internalization.

More adverse impacts, like the steeper decline in metabolic function with increasing WS_2 concentration (**Fig. 2**), more substantial cell morphological alterations (**Fig. S-11**), stronger lipid peroxidation in mitochondria, and more reductions in $\Delta\Psi_m$[56] (**Fig. S21-22**), were observed in BEAS-2B cells relative to the tumorigenic A549. Additionally, while oligomycin-like inhibition of mitochondria function[57] was found in both cells, the nanosheets completely blocked mitochondrial respiration in BEAS-2B but not in A549 cells (**Figs. 4 and 5**). The higher cellular uptake and more appreciable association of the nanosheets with mitochondria in BEAS-2B cells may have contributed to such differences. Moreover, clathrin-mediated endocytosis, which was essential for nanosheet uptake in BEAS-2B cells, may be transporting the nanosheets directly to mitochondria[58], making BEAS-2B much more sensitive to WS_2 than the tumorigenic A549.

However, our study has far been conclusive in determination of the PCD mechanisms caused by low-dose exposure to WS_2 nanosheets. For example, our results on caspase-8 were inconclusive, and probably complicated by the onset of necrosis with longer exposure times or higher doses, since caspase-8 activation is tightly regulated in cells and involved in both apoptosis and necrosis[54]. More studies employing advanced multi-omics tools are needed to comprehensively document all potential impacts by the nanosheets on the cells, and reveal the activation of multiple types of PCD mechanisms[59]. Nevertheless, the adverse biological impacts induced by low dose exposures of WS_2 nanosheets in human lung epithelial cells, and the differential impacts to the normal and tumorigenic cells found in our work, supports the importance for additional nanotoxicological and *in vivo* inhalation studies, focused on assessing currently established occupational PELs.

ASSOCIATED CONTENT

Supporting Information.

The following files are available free of charge. Additional experimental procedures; supplemental material characterization data; cell metabolic function test with PF108; assessment of cell membrane integrity and LDH leakage; lysosome and mitochondria imaging in cells; ICP-OES data; O_2 tension profiles; cellular respiration measurements, immunoblots.

AUTHOR INFORMATION

Corresponding Author

* Prof. Wenwan Zhong, Email: wenwan.zhong@ucr.edu

Notes

The authors declare no competing financial interest.

ACKNOWLEDGMENT

This study was supported by the National Institute of Environmental Health Sciences (NIEHS) (No. U01ES027293) as part of the NHIR Consortium. The Engineered Nanomaterials Resource and Coordination Core at the Harvard T.H. Chan School of Public Health (HSPH), (NIEHS No. U24ES026946), synthesized the WS_2 nanosheets. R.C. was supported by the Research Training Grant in Environmental Toxicology (NIEHS No. T32ES018827). This work was supported by the UCR Stem Cell Core Facility. The graphical abstract was made with BioRender. The authors would like to thank Professor Markita Landry for supporting this work, Professor Ying-Hsuan Lin for generously providing BEAS-2B cells, and the Brooks Lab at UC Berkeley for sharing their Seahorse XFp analyzer.

REFERENCES

(1) Mak, K. F.; Shan, J. Photonics and Optoelectronics of 2D Semiconductor Transition Metal Dichalcogenides. *Nat. Photonics* **2016**, *10* (4), 216–226. https://doi.org/10.1038/nphoton.2015.282.

(2) Kim, H. C.; Kim, H.; Lee, J. U.; Lee, H. B.; Choi, D. H.; Lee, J. H.; Lee, W. H.; Jhang, S. H.; Park, B. H.; Cheong, H.; Lee, S. W.; Chung, H. J. Engineering Optical and Electronic Properties of WS2 by Varying the Number of Layers. *ACS Nano* **2015**, *9* (7), 6854–6860. https://doi.org/10.1021/acsnano.5b01727.

(3) Chhowalla, M.; Shin, H. S.; Eda, G.; Li, L. J.; Loh, K. P.; Zhang, H. The Chemistry of Two-Dimensional Layered Transition Metal Dichalcogenide Nanosheets. *Nat. Chem.* **2013**, *5* (4), 263–275. https://doi.org/10.1038/nchem.1589.

(4) Lei, W.; Xiao, J.-L.; Liu, H.-P.; Jia, Q.-L.; Zhang, H.-J. Tungsten Disulfide: Synthesis and Applications in Electrochemical Energy Storage and Conversion. *Tungsten* **2020**, *2* (3), 217–239. https://doi.org/10.1007/s42864-020-00054-6.

(5) He, X.; Iwamoto, Y.; Kaneko, T.; Kato, T. Fabrication of Near-Invisible Solar Cell with Monolayer WS2. *Sci. Rep.* **2022**, *12* (1), 11315. https://doi.org/10.1038/s41598-022-15352-x.

(6) Niste, V. B.; Ratoi, M.; Tanaka, H.; Xu, F.; Zhu, Y.; Sugimura, J. Self-Lubricating Al-WS2 Composites for Efficient and Greener Tribological Parts. *Sci. Rep.* **2017**, *7* (1), 1–14. https://doi.org/10.1038/s41598-017-15297-6.

(7) Ding, J.; Feng, A.; Li, X.; Ding, S.; Liu, L.; Ren, W. Properties, Preparation, and Application of Tungsten Disulfide: A Review. *J. Phys. Appl. Phys.* **2021**, *54* (17). https://doi.org/10.1088/1361-6463/abd9e8.

(8) Zhao, L.; Lu, L.; Wang, A.; Zhang, H.; Huang, M.; Wu, H.; Xing, B.; Wang, Z.; Ji, R. Nano-Biotechnology in Agriculture: Use of Nanomaterials to Promote Plant Growth and Stress Tolerance. *J. Agric. Food Chem.* **2020**, *68* (7), 1935–1947. https://doi.org/10.1021/acs.jafc.9b06615.

(9) An, C.; Sun, C.; Li, N.; Huang, B.; Jiang, J.; Shen, Y.; Wang, C.; Zhao, X.; Cui, B.; Wang, C.; Li, X.; Zhan, S.; Gao, F.; Zeng, Z.; Cui, H.; Wang, Y. Nanomaterials and Nanotechnology for the Delivery of Agrochemicals: Strategies towards Sustainable Agriculture. *J. Nanobiotechnology* **2022**, *20* (1), 1–19. https://doi.org/10.1186/s12951-021-01214-7.

(10) Agarwal, V.; Chatterjee, K. Recent Advances in the Field of Transition Metal Dichalcogenides for Biomedical Applications. *Nanoscale* **2018**, *10* (35), 16365–16397. https://doi.org/10.1039/c8nr04284e.

(11) Cheng, L.; Yuan, C.; Shen, S.; Yi, X.; Gong, H.; Yang, K.; Liu, Z. Bottom-Up Synthesis of Metal-Ion-Doped WS2 Nanoflakes for Cancer Theranostics. *ACS Nano* **2015**, *9* (11), 11090–11101. https://doi.org/10.1021/acsnano.5b04606.

(12) So, Y.; Yim, D. B.; Son, W.; Lee, H.; Lee, S.; Choi, C.; Yang, C. S.; Kim, J. H. Deciphering the Therapeutic Mechanism of Topical WS2 Nanosheets for the Effective Therapy of Burn Injuries. *Appl. Mater. Today* **2022**, *29* (July), 101591–101591. https://doi.org/10.1016/j.apmt.2022.101591.

(13) Klasson, M.; Bryngelsson, I.-L.; Pettersson, C.; Husby, B.; Arvidsson, H.; Westberg, H. Occupational Exposure to Cobalt and Tungsten in the Swedish Hard Metal Industry: Air Concentrations of Particle Mass, Number, and Surface Area. *Ann. Occup. Hyg.* **2016**, *60* (6), 684–699. https://doi.org/10.1093/annhyg/mew023.

(14) Lemus, R.; Venezia, C. F. An Update to the Toxicological Profile for Water-Soluble and Sparingly Soluble Tungsten Substances. *Crit. Rev. Toxicol.* **2015**, *45* (5), 388–411. https://doi.org/10.3109/10408444.2014.1003422.

(15) Teo, W. Z.; Chng, E. L. K.; Sofer, Z.; Pumera, M. Cytotoxicity of Exfoliated Transition-Metal Dichalcogenides (MoS 2, WS2, and WSe2) Is Lower than That of Graphene and Its Analogues. *Chem. - Eur. J.* **2014**, *20* (31), 9627–9632. https://doi.org/10.1002/chem.201402680.

(16) Yuan, P.; Zhou, Q.; Hu, X. WS2 Nanosheets at Noncytotoxic Concentrations Enhance the Cytotoxicity of Organic Pollutants by Disturbing the Plasma Membrane and Efflux Pumps. *Environ. Sci. Technol.* **2020**, *54* (3), 1698–1709. https://doi.org/10.1021/acs.est.9b05537.

(17) Cheng, L.; Liu, J.; Gu, X.; Gong, H.; Shi, X.; Liu, T.; Wang, C.; Wang, X.; Liu, G.; Xing, H.; Bu, W.; Sun, B.; Liu, Z. PEGylated WS2 Nanosheets as a Multifunctional Theranostic Agent for in Vivo Dual-Modal CT/Photoacoustic Imaging Guided Photothermal Therapy. *Adv. Mater.* **2014**, *26* (12), 1886–1893. https://doi.org/10.1002/adma.201304497.

(18) Xu, S.; Zheng, H.; Ma, R.; Wu, D.; Pan, Y.; Yin, C.; Gao, M.; Wang, W.; Li, W.; Liu, S.; Chai, Z.; Li, R. Vacancies on 2D Transition Metal Dichalcogenides Elicit Ferroptotic Cell Death. *Nat. Commun.* **2020**, *11* (1), 1–14. https://doi.org/10.1038/s41467-020-17300-7.

(19) Bazina, L.; Bitounis, D.; Cao, X.; Deloid, G. M.; Parviz, D.; Strano, M. S.; Lin, H. Y. G.; Bell, D. C.; Thrall, B. D.; Demokritou, P. Biotransformations and Cytotoxicity of Graphene and Inorganic Two-Dimensional Nanomaterials Using Simulated Digestions Coupled with a Triculture: In Vitro Model of the Human Gastrointestinal Epithelium. *Environ. Sci. Nano* **2021**, *8* (11), 3233–3249. https://doi.org/10.1039/d1en00594d.

(20) Guiney, L. M.; Wang, X.; Xia, T.; Nel, A. E.; Hersam, M. C. Assessing and Mitigating the Hazard Potential of Two-Dimensional Materials. *ACS Nano* **2018**, *12* (7), 6360–6377. https://doi.org/10.1021/acsnano.8b02491.

(21) Cai, X.; Liu, X.; Jiang, J.; Gao, M.; Wang, W.; Zheng, H.; Xu, S.; Li, R. Molecular Mechanisms, Characterization Methods, and Utilities of Nanoparticle Biotransformation in Nanosafety Assessments. *Small* **2020**, *16* (36), 1–19. https://doi.org/10.1002/smll.201907663.

(22) *Tungsten, Metal & Insoluble Compounds*. OSHA Occupational Chemical Database. https://www.osha.gov/chemicaldata/524 (accessed 2023-02-02).

(23) NIOSH. *Current Intelligence Bulletin 70: Health Effects of Occupational Exposure to Silver Nanomaterials*; DHHS (NIOSH) Publication No. 2021-112; NIOSH, 2021. https://www.cdc.gov/niosh/docs/2021-112/pdfs/2021-112.pdf?id=10.26616/NIOSHPUB2021112 (accessed 2023-02-02).

(24) NIOSH. *Current Intelligence Bulletin 65: Occupational Exposure to Carbon Nanotubes and Nanofibers*; DHHS (NIOSH) Publication No. 2013–145; NIOSH, 2013. https://www.cdc.gov/niosh/docs/2013-145/pdfs/2013-145.pdf.

(25) Cai, X.; Lee, A.; Ji, Z.; Huang, C.; Chang, C. H.; Wang, X.; Liao, Y. P.; Xia, T.; Li, R. Reduction of Pulmonary Toxicity of Metal Oxide Nanoparticles by Phosphonate-Based Surface Passivation. *Part. Fibre Toxicol.* **2017**, *14*. https://doi.org/10.1186/s12989-017-0193-5.

(26) DeLoid, G.; Cohen, J. M.; Darrah, T.; Derk, R.; Rojanasakul, L.; Pyrgiotakis, G.; Wohlleben, W.; Demokritou, P. Estimating the Effective Density of Engineered Nanomaterials for in Vitro Dosimetry. *Nat. Commun.* **2014**, *5* (1), 3514. https://doi.org/10.1038/ncomms4514.

(27) Parviz, D.; Bitounis, D.; Demokritou, P.; Strano, M. Engineering Two-Dimensional Nanomaterials to Enable Structure-Activity Relationship Studies in Nanosafety Research. *NanoImpact* **2020**, *18*, 100226. https://doi.org/10.1016/j.impact.2020.100226.

(28) Ma-Hock, L.; Sauer, U. G.; Ruggiero, E.; Keller, J.; Wohlleben, W.; Landsiedel, R. The Use of Nanomaterial In Vivo Organ Burden Data for In Vitro Dose Setting. *Small* **2021**, *17* (15), 2005725. https://doi.org/10.1002/smll.202005725.

(29) Yang, D.; Frindt, R. F. Li-Intercalation and Exfoliation of WS2. *J. Phys. Chem. Solids* **1996**, *57* (6–8), 1113–1116. https://doi.org/10.1016/0022-3697(95)00406-8.

(30) Hadrup, N.; Sørli, J. B.; Sharma, A. K. Pulmonary Toxicity, Genotoxicity, and Carcinogenicity Evaluation of Molybdenum, Lithium, and Tungsten: A Review. *Toxicology* **2022**, *467* (153098). https://doi.org/10.1016/j.tox.2022.153098.

(31) Faber, S. C.; McCullough, S. D. Through the Looking Glass: In Vitro Models for Inhalation Toxicology and Interindividual Variability in the Airway. *Appl. Vitro Toxicol.* **2018**, *4* (2), 115–128. https://doi.org/10.1089/aivt.2018.0002.

(32) Hajam, Y. A.; Rani, R.; Ganie, S. Y.; Sheikh, T. A.; Javaid, D.; Qadri, S. S.; Pramodh, S.; Alsulimani, A.; Alkhanani, M. F.; Harakeh, S.; Hussain, A.; Haque, S.; Reshi, M. S. Oxidative Stress in Human Pathology and Aging: Molecular Mechanisms and Perspectives. *Cells* **2022**, *11* (3), 552. https://doi.org/10.3390/cells11030552.

(33) Lin, T.; Zhong, L.; Song, Z.; Guo, L.; Wu, H.; Guo, Q.; Chen, Y.; Fu, F.; Chen, G. Visual Detection of Blood Glucose Based on Peroxidase-like Activity of WS2 Nanosheets. *Biosens. Bioelectron.* **2014**, *62*, 302–307. https://doi.org/10.1016/j.bios.2014.07.001.

(34) Yu, Y.; Yan, Y.; Niu, F.; Wang, Y.; Chen, X.; Su, G.; Liu, Y.; Zhao, X.; Qian, L.; Liu, P.; Xiong, Y. Ferroptosis: A Cell Death Connecting Oxidative Stress, Inflammation and Cardiovascular Diseases. *Cell Death Discov.* **2021**, *7* (1), 193. https://doi.org/10.1038/s41420-021-00579-w.

(35) Aoki, K.; Satoi, S.; Harada, S.; Uchida, S.; Iwasa, Y.; Ikenouchi, J. Coordinated Changes in Cell Membrane and Cytoplasm during Maturation of Apoptotic Bleb. *Mol. Biol. Cell* **2020**, *31* (8), 833–844. https://doi.org/10.1091/mbc.E19-12-0691.

(36) Zhang, Y.; Chen, X.; Gueydan, C.; Han, J. Plasma Membrane Changes during Programmed Cell Deaths. *Cell Res.* **2018**, *28* (1), 9–21. https://doi.org/10.1038/cr.2017.133.

(37) Ferranti, C. S.; Cheng, J.; Thompson, C.; Zhang, J.; Rotolo, J. A.; Buddaseth, S.; Fuks, Z.; Kolesnick, R. N. Fusion of Lysosomes to Plasma Membrane Initiates Radiation-Induced Apoptosis. *J. Cell Biol.* **2020**, *219* (4), e201903176. https://doi.org/10.1083/jcb.201903176.

(38) Su, C. F.; Merlitz, H.; Thalmann, F.; Marques, C.; Sommer, J. U. Coarse-Grained Model of Oxidized Membranes and Their Interactions with Nanoparticles of Various Degrees of Hydrophobicity. *J. Phys. Chem. C* **2019**, *123* (11), 6839–6848. https://doi.org/10.1021/acs.jpcc.8b11909.

(39) Rennick, J. J.; Johnston, A. P. R.; Parton, R. G. Key Principles and Methods for Studying the Endocytosis of Biological and Nanoparticle Therapeutics. *Nat. Nanotechnol.* **2021**, *16* (3), 266–276. https://doi.org/10.1038/s41565-021-00858-8.

(40) Zeng, X.; Zhang, Y.; Nyström, A. M. Endocytic Uptake and Intracellular Trafficking of Bis-MPA-Based Hyperbranched Copolymer Micelles in Breast Cancer Cells. *Biomacromolecules* **2012**, *13* (11), 3814–3822. https://doi.org/10.1021/bm301281k.

(41) Takahashi, S.; Tada, R.; Negishi, Y.; Aramaki, Y. Mechanisms of Enhanced Antigen Delivery to Murine Dendritic Cells by the Cationic Liposomes. *Open J. Immunol.* **2017**, *07* (04), 85–101. https://doi.org/10.4236/oji.2017.74007.

(42) dos Santos, T.; Varela, J.; Lynch, I.; Salvati, A.; Dawson, K. A. Effects of Transport Inhibitors on the Cellular Uptake of Carboxylated Polystyrene Nanoparticles in Different Cell Lines. *PLoS ONE* **2011**, *6* (9). https://doi.org/10.1371/journal.pone.0024438.

(43) Gallud, A.; Klöditz, K.; Ytterberg, J.; Östberg, N.; Katayama, S.; Skoog, T.; Gogvadze, V.; Chen, Y.-Z.; Xue, D.; Moya, S.; Ruiz, J.; Astruc, D.; Zubarev, R.; Kere, J.; Fadeel, B. Cationic Gold Nanoparticles Elicit Mitochondrial Dysfunction: A Multi-Omics Study. *Sci. Rep.* **2019**, *9* (1), 4366. https://doi.org/10.1038/s41598-019-40579-6.

(44) Qiu, K.; Zou, W.; Fang, Z.; Wang, Y.; Bell, S.; Zhang, X.; Tian, Z.; Xu, X.; Ji, B.; Li, D.; Huang, T.; Diao, J. 2D MoS_2 and BN Nanosheets Damage Mitochondria through Membrane Penetration. *ACS Nano* **2023**, acsnano.2c11003. https://doi.org/10.1021/acsnano.2c11003.

(45) Gao, M.; Yi, J.; Zhu, J.; Minikes, A. M.; Monian, P.; Thompson, C. B.; Jiang, X. Role of Mitochondria in Ferroptosis. *Mol. Cell* **2019**, *73* (2), 354-363.e3. https://doi.org/10.1016/j.molcel.2018.10.042.

(46) Spinelli, J. B.; Haigis, M. C. The Multifaceted Contributions of Mitochondria to Cellular Metabolism. *Nat. Cell Biol.* **2018**, *20* (7), 745–754. https://doi.org/10.1038/s41556-018-0124-1.

(47) Chen, Y.; Zhou, Z.; Min, W. Mitochondria, Oxidative Stress and Innate Immunity. *Front. Physiol.* **2018**, *9*, 1487. https://doi.org/10.3389/fphys.2018.01487.

(48) Divakaruni, A. S.; Jastroch, M. A Practical Guide for the Analysis, Standardization and Interpretation of Oxygen Consumption Measurements. *Nat. Metab.* **2022**, *4* (8), 978–994. https://doi.org/10.1038/s42255-022-00619-4.

(49) Wang, L.; Mello, D. F.; Zucker, R. M.; Rivera, N. A.; Rogers, N. M. K.; Geitner, N. K.; Boyes, W. K.; Wiesner, M. R.; Hsu-Kim, H.; Meyer, J. N. Lack of Detectable Direct Effects of Silver and Silver Nanoparticles on Mitochondria in Mouse Hepatocytes. *Environ. Sci. Technol.* **2021**, *55* (16), 11166–11175. https://doi.org/10.1021/acs.est.1c02295.

(50) Coreas, R.; Castillo, C.; Li, Z.; Yan, D.; Gao, Z.; Chen, J.; Bitounis, D.; Parviz, D.; Strano, M. S.; Demokritou, P.; Zhong, W. Biological Impacts of Reduced Graphene Oxide Affected by Protein Corona Formation. *Chem. Res. Toxicol.* **2022**, *35* (7), 1244–1256. https://doi.org/10.1021/acs.chemrestox.2c00042.

(51) Demine, S.; Renard, P.; Arnould, T. Mitochondrial Uncoupling: A Key Controller of Biological Processes in Physiology and Diseases. *Cells* **2019**, *8* (8). https://doi.org/10.3390/cells8080795.

(52) Kupcho, K.; Shultz, J.; Hurst, R.; Hartnett, J.; Zhou, W.; Machleidt, T.; Grailer, J.; Worzella, T.; Riss, T.; Lazar, D.; Cali, J. J.; Niles, A. A Real-Time, Bioluminescent Annexin V Assay for the Assessment of Apoptosis. *Apoptosis* **2019**, *24*, 184–197. https://doi.org/10.1007/s10495-018-1502-7.

(53) Galluzzi, L.; Vitale, I. Molecular Mechanisms of Cell Death: Recommendations of the Nomenclature Committee on Cell Death 2018. *Cell Death Differ.* **2018**, *25* (3), 486–541. https://doi.org/10.1038/s41418-017-0012-4.

(54) McIlwain, D. R.; Berger, T.; Mak, T. W. Caspase Functions in Cell Death and Disease. *Cold Spring Harb. Perspect. Biol.* **2013**, *5* (4), a008656–a008656. https://doi.org/10.1101/cshperspect.a008656.

(55) Wilson, T. R.; Redmond, K. M.; McLaughlin, K. M.; Crawford, N.; Gately, K.; O'Byrne, K.; Le-Clorrenec, C.; Holohan, C.; Fennell, D. A.; Johnston, P. G.; Longley, D. B. Procaspase 8 Overexpression in Non-Small-Cell Lung Cancer Promotes Apoptosis Induced by FLIP Silencing. *Cell Death Differ.* **2009**, *16* (10), 1352–1361. https://doi.org/10.1038/cdd.2009.76.

(56) Zorova, L. D.; Popkov, V. A.; Plotnikov, E. Y.; Silachev, D. N.; Pevzner, I. B.; Jankauskas, S. S.; Babenko, V. A.; Zorov, S. D.; Balakireva, A. V.; Juhaszova, M.; Sollott, S. J.; Zorov, D. B. Mitochondrial Membrane Potential. *Anal. Biochem.* **2018**, *552*, 50–59. https://doi.org/10.1016/j.ab.2017.07.009.

(57) Hearne, A.; Chen, H.; Monarchino, A.; Wiseman, J. S. Oligomycin-Induced Proton Uncoupling. *Toxicol. In Vitro* **2020**, *67*, 104907. https://doi.org/10.1016/j.tiv.2020.104907.

(58) Wei, Z.; Su, W.; Lou, H.; Duan, S.; Chen, G. Trafficking Pathway between Plasma Membrane and Mitochondria via Clathrin-Mediated Endocytosis. *J. Mol. Cell Biol.* **2018**, *10* (6), 539–548. https://doi.org/10.1093/jmcb/mjy060.

(59) Lomphithak, T.; Fadeel, B. Die Hard: Cell Death Mechanisms and Their Implications in Nanotoxicology. *Toxicol. Sci.* **2023**, kfad008. https://doi.org/10.1093/toxsci/kfad008.

Supplementary Information:

Low Dose Exposure of WS_2 Nanosheets Induces Differential Apoptosis in Lung Epithelial Cells

*Roxana Coreas[1], Zongbo Li[2], Junyi Chen[1], Wenwan Zhong[1,2]**

[1]Environmental Toxicology Graduate Program; [2]Department of Chemistry, University of California-Riverside, Riverside, CA 92521, USA

* Corresponding author

Prof. Wenwan Zhong, email: wenwan.zhong@ucr.edu

Table of Contents

FIGURES

MATERIALS AND METHODS

Source of materials. WS_2 nanosheets were synthesized by the Nanotechnology Health Implications Research consortium at the Harvard HSPH-NIEHS Nanosafety Center[1]. Hoechst 33342, 5-(and-6)-chloromethyl-2',7'-dichlorofluorescein diacetate (CM-H_2DCF-DA), 2',7'-dichlorofluorescein diacetate (H_2DCF-DA), chlorpromazine hydrochloride, cytochalasin D, genistein, Image-iT lipid peroxidation kit, mitochondria isolation kit for cultured cells, bicinchoninic acid (BCA), SuperSignal West Pico Plus, and the CyQUANT LDH cytotoxicity assay kit were purchased from Thermo Fisher Scientific (Waltham, MA, USA). CCK-8 was purchased from BiMake (Houston, TX, USA). Bronchial Epithelial Cell Growth Basal Medium (BEBM) was purchased from Lonza (Basel, Switzerland). Phosphate buffered saline (1 × PBS, pH 7.4), Ham's F-12K (Kaighn's) Medium, penicillin-streptomycin (1000 U/mL), and fetal bovine serum (FBS), were manufactured by Gibco (Waltham, MA, USA). Mitochondria membrane potential (MMP) kit was acquired from Sigma-Aldrich (St. Louis, MO, USA). RealTime-Glo Annexin V Apoptosis & Necrosis Assay, and secondary antibody (anti-rabbit IgG (H+L) HRP conjugated) were purchased from Promega (Madison, WI, USA). Primary antibodies for cytochrome-*c*, caspase 3, caspase 9, and GAPDH (rabbit polyclonal) were purchased from Sino Biological. The caspase 8 antibody (rabbit polyclonal) was acquired from Proteintech.

WS_2 Characterization. A Thermo Scientific Talos L120C TEM and a Thermo Scientific Titan Themis 300 STEM equipped with a Super-X EDS system used for elemental analysis were employed to examine the nanosheets. WS_2 nanosheets were dropped onto 200-mesh copper grids with holey carbon support films and dried under ambient conditions prior to imaging. For AFM, WS_2 nanosheets were diluted in ethanol, dropped onto a Si wafer, and dried under ambient conditions. The Si wafer was first cleaned with H_2SO_4/H_2O_2 (3:1) overnight, washed with acetone and ethanol 3·, then treated with (3-aminopropyl)triethoxysilane (APTES) overnight to attach amine groups to its surface. AFM imaging was performed with a Bruker VEECO D3100 Nanoman AFM, with images acquired in tapping mode, using the MESP-V2 probe (Bruker). The scanning rate was 1 Hz, with integral gain of 0.2 and proportional gain of 0.4. The amplitude set-point was set at 1.250 V, and the tip velocity was 6 μm/s. Image analysis was performed with NanoScope V530r3sr3 (Bruker).The hydrodynamic diameter (D_H) was measured with a Nanosight NS300 from Malvern Panalytical using a low-volume flow cell manifold. Sixty second videos were collected in triplicate and the WS_2 Brownian motion was analyzed with the Malvern NTA 3.3. software. Zeta (ζ) potentials and dynamic light scattering size measurements were measured with a Malvern Zetasizer (Nano ZS) and DTS1070 zeta cell. Surface functional groups were analyzed using a Thermo Nicolet 6700 FTIR. WS_2 absorbance was measured with an Agilent Cary 60 UV-Vis spectrophotometer.

Cell culture. Alveolar basal epithelial cancer cells (A549) and non-tumorigenic lung epithelial cells (BEAS-2B) were cultured in Ham's F-12K Medium (supplemented with 10% FBS and 1% penicillin/streptomycin) and supplemented BEBM, respectively. Cells were grown in a humidified incubator at 37°C, 5%. CO_2, regularly screened for mycoplasma contamination, and transferred to well plates for exposure experiments once cells reached confluency (~80%).

WS_2 suspensions in cell culture media (CCM). Aliquots of WS_2 nanosheets, suspended in 10 mg/mL PF108, were diluted in CCM to a concentration of 100 µg/mL, inverted 5×, and incubated in a warm water bath (37°C) for 1 hour (h). After the incubation, the solutions were inverted 5×, diluted into working stocks with fresh CCM and subsequently pipetted into wells containing cultured cells.

LDH leakage assay. Cells were seeded and grown as mentioned above. Following WS_2 exposure, 50 µL of the supernatants were transferred to a new well plate, mixed with the Reaction Mix solution (Invitrogen's CyQUANT LDH cytotoxicity assay), and incubated in dark ambient conditions for 30 min. The reaction was stopped and the absorbances at 490 and 680 nm were measured with a Promega Glomax plate reader. The LDH activity was calculated by taking the difference in absorbance (A_{490}-A_{680}).

Viability (Trypan blue) assay. Cells, grown in clear 6-well plates with initial seeding densities of 2×10^5 cells/well, were dosed with 0, 1, 5, 10, 50, and 100 µg/mL of WS_2 nanosheets for 24 h. Following exposure, cells were washed 2× with cold 1× PBS, and detached from the plate using a 0.25% trypsin-EDTA solution. Cells were pelleted to remove the trypsinization solution and were resuspended in 1mL of fresh CCM. An aliquot (10 µL) was diluted with Trypan blue (1:1 v/v) and cells were counted with a TC20 automated cell counter (BioRad).

Metabolically active cells (CCK8) assay. Cells, grown in clear 96-well plates with initial seeding densities of 1×10^4 cells/well, were dosed with 0, 0.1, 0.5, 1, 5, 10, 20, 50, & 100 µg/mL of WS_2 nanosheets for 24 h. Following exposure, cells were washed 2× with cold 1× PBS, and fresh media was introduced into the wells with the CCK-8 reagent. Following a 1-h incubation at 37°C, the absorbance at 450 nm was measured with a Biotek plate reader. Cytotoxicity was calculated by subtracting the background signal and normalizing to the unexposed control.

Cell ROS assay. Cells were seeded in black 96-well plates at a density of 1×10^4 cells/well. Following the same treatment and washing steps mentioned above, cells were exposed to either 2× Deep Red or 5 µM CM-H_2DCF-DA (in 1× PBS) for 30 min. The loading probe solution was removed and replaced with CCM to allow for a 30 min recovery period. The fluorescent signal was measured using bottom read mode at 650/675 and 485/528 nm (ex/em), respectively, with a Tecan plate reader. Fluorescence intensities were normalized to the untreated control (F_0), (i.e. F/F_0).

Abiotic ROS assay. H_2DCF-DA was deacetylated in CCM with 10% FBS for 30 min at 37°C. WS_2 nanosheets were plated into a black-bottom 96-well plate and loaded into a GloMax plate reader. The activated dye was injected into each well. The final concentrations for H_2DCF was 1 µM. After 10 min in dark conditions, the fluorescence of the DCF dye was measured at 488/525 nm (ex/em).

Lipid membrane peroxidation. Cells were seeded in black with clear-bottom 96-well plates (1×10^4 cells/well). Following 24 h exposures to either 0, 5, or 50 µg/mL WS_2, cells were washed 2× with 1× PBS and stained 20 min with 10 µM Image-iT Lipid Peroxidation Sensor and 5 µM Hoechst 33342. The dyes were removed and cells were washed 2× with cold 1× PBS. Cells exposed to 100 µM cumene hydroperoxide for 1 h served as the positive control. Imaging was accomplished with a Nikon Eclipse Ti inverted microscope using Texas Red & FITC filters. Cellular fluorescence intensities were analyzed with ImageJ2 software (version: 2.3.0/1.53q).

Mitochondria membrane potential. Cells were seeded in 6-well plates (2×10^5 cells/well). Following 24-h exposures to 0, 10, or 50 µg/mL WS_2, cells were washed 2× with 1× PBS and stained for 20 minutes with 1× Mitochondrial Membrane Potential Dye (Sigma Aldrich). Cells were detached and pelleted by centrifugation at 500 *g* for 5 minutes. Cells were resuspended in ice-cold 1× PBS, strained to obtain a uniform single cell suspension, and analyzed with an ACEA NovoCyte flow cytometer using the FITC channel (λ_{em} = 535 nm). For each condition 100,000 events were collected and analyzed with the Agilent NovoExpress software.

Cellular uptake measurement with ICP-OES (continued). An internal standard, yttrium (2.5 ppm), was added to the sample stream between the autosampler and the nebulizer. The RF frequency was 1350 Watts. The autosampler rate was 0.8 mL/min. Argon flow rates for plasma, the auxiliary, and the nebulizer were 15, 0.2, and 0.5 L/min, respectively. To calculate cell and mitochondria uptake, background signals from untreated cells, or mitochondria, (x) were subtracted from the concentrations measured in WS_2 treated cells, or mitochondria, (y) and the values were normalized to cell-free WS_2 nanosheet controls digested at the respective concentrations (z), with Eq. 1:

$$(1)\ \%\ uptake = \left(\frac{Y_{ppm} - X_{ppm}}{Z_{ppm}}\right)$$

Real-time apoptosis and necrosis assay. Cells were seeded in black, clear-bottom, 96-well plates with a density of 1×10^4 cells/well. The 2× Detection Reagent was aliquoted and Annexin NanoBit Substrate, $CaCl_2$, Necrosis Detection Reagent, Annexin V-SmBiT and the Annexin V-LgBiT were added at a 500-fold dilution. The original culture media in the wells was removed, and 100 µL aliquots of 2× the desired starting concentration of WS_2 were prepared and added to the wells. To these wells, 100 µL of the 2× Detection Reagent mixture was added and immediately after luminescence and fluorescence were measured (t = 0). Measurements were subsequently made at 6, 12, and 24 h. Background controls, WS_2 in cell culture media without cells, were measured and subtracted from the exposed cell measurements.

Immunoblotting. After cells were treated with WS_2 nanosheets, they were placed on ice and washed 2× with cold 1× PBS. Cells were lysed with 200 µL of 2× Laemmli buffer supplemented with 2-mercaptoethanol. Lysate solutions were transferred to cold microcentrifuge tubes and vortexed every 10 min for 1 h. Protein concentration was determined with BCA. Cell lysates were boiled for 5 mins, separated on 12% SDS-PAGE gels at 100 V, and transferred to nitrocellulose membranes via semi-dry method for 45 min. Blotted membranes were blocked with 3% bovine serum albumin (BSA) in Tris-buffered saline with 1:1000 Tween (TBST) for 12 h with agitation at 4 ℃. The blots were rinsed 3× with TBST for 5 min/rinse, then incubated with primary antibody solutions (primary antibody diluted in 3% BSA in TBST, 0.1% NaN_3) for 8 h with agitation at 4 ℃. Blots were rinsed 3× with TBST for 3 min/rinse and incubated with secondary antibody solutions (secondary antibody diluted in 3% BSA in TBST, 0.1% NaN_3) for 1 h with agitation at ambient temperature. Unbound secondary antibodies were removed by washing blots 3× with TBST for 3 min/rinse. SuperSignal West Pico Plus was used for the chemiluminescent substrate and blots were imaged on a Li-COR Fc.

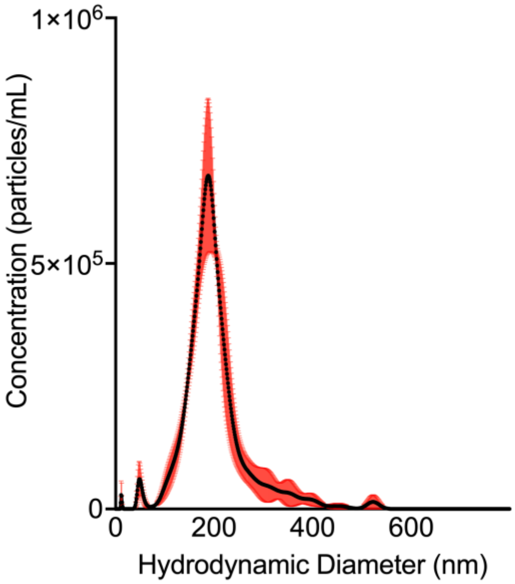

Figure S-1. Hydrodynamic diameter (D_H) of WS_2 nanosheets measured by NTA.The D_H was 195 ± 13 nm. The black line represents the mean (n=3) and the red outline shows SD.

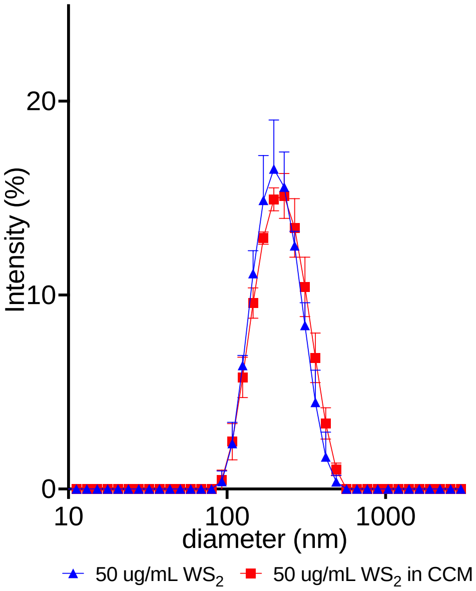

Figure S-2. The D_H of WS_2 nanosheets, measured by DLS. The D_H was 199 ± 24 nm. The blue line represents the average (n=3) measurement of WS_2 in water. The red line represents the average measurement of WS_2 prepared in cell culture media supplemented with 10% FBS.

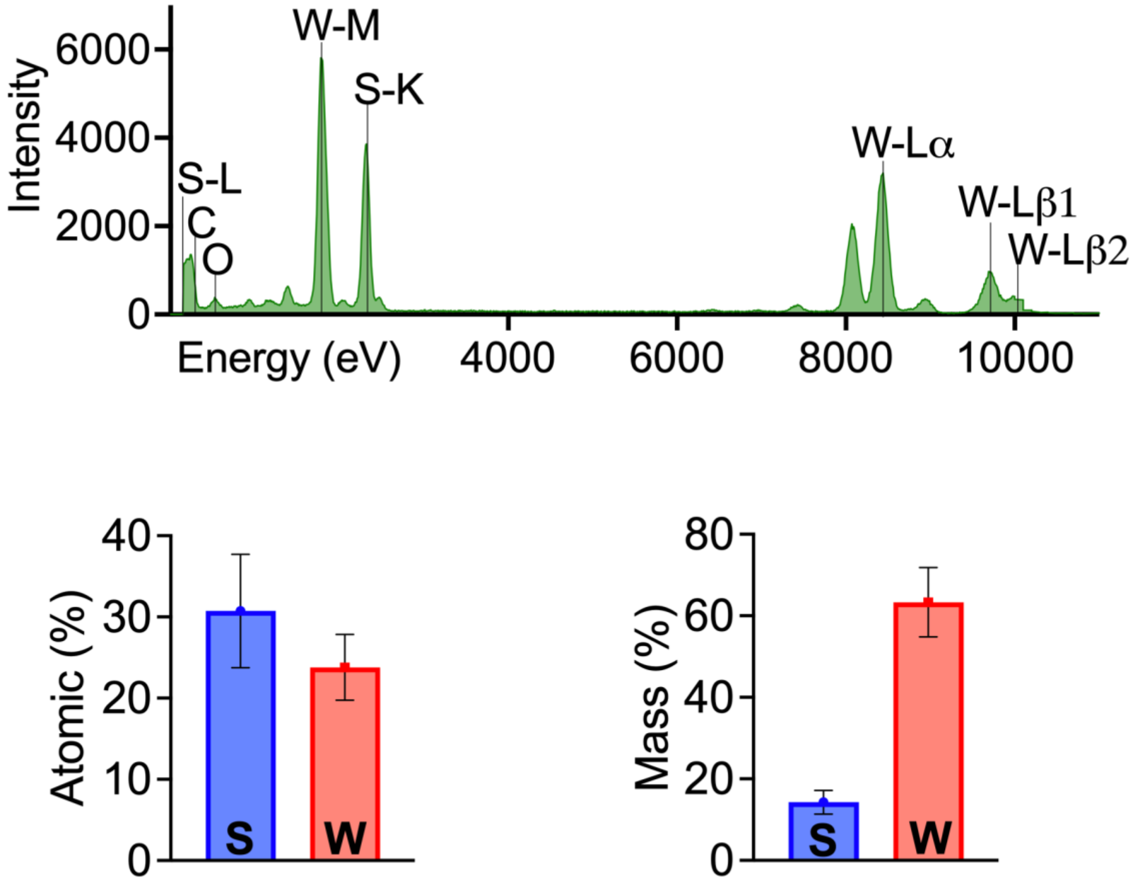

Figure S-3. EDS spectra of WS_2 nanosheets. Atomic and mass fractions of WS_2 are shown as bar plots. Each bar represents the mean ± SEM.

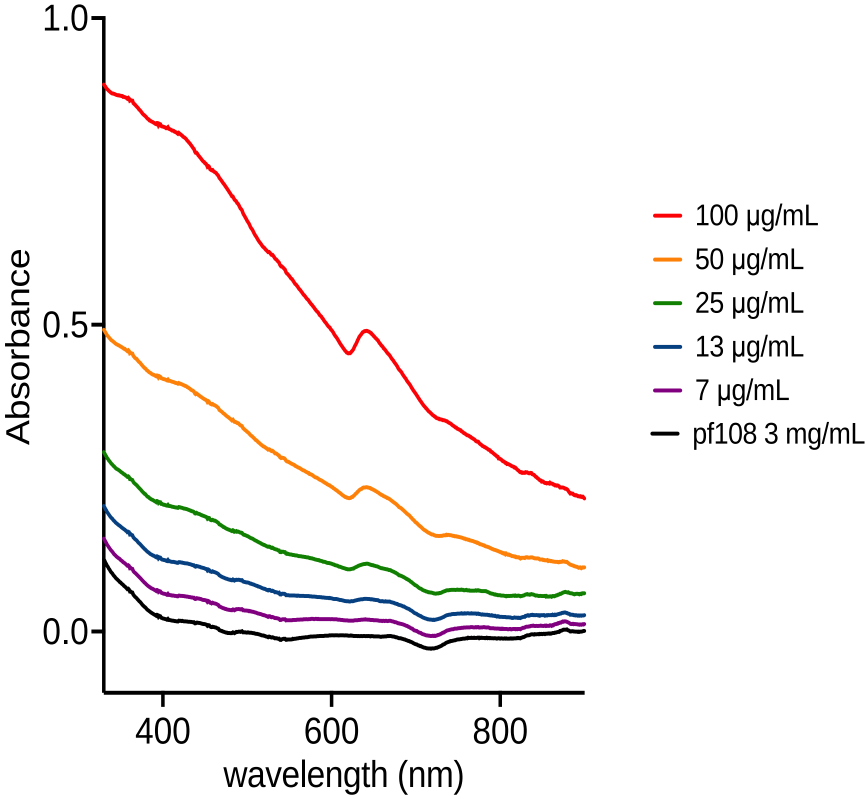

Figure S-4. UV-Vis spectra of WS_2 nanosheets at different concentrations.

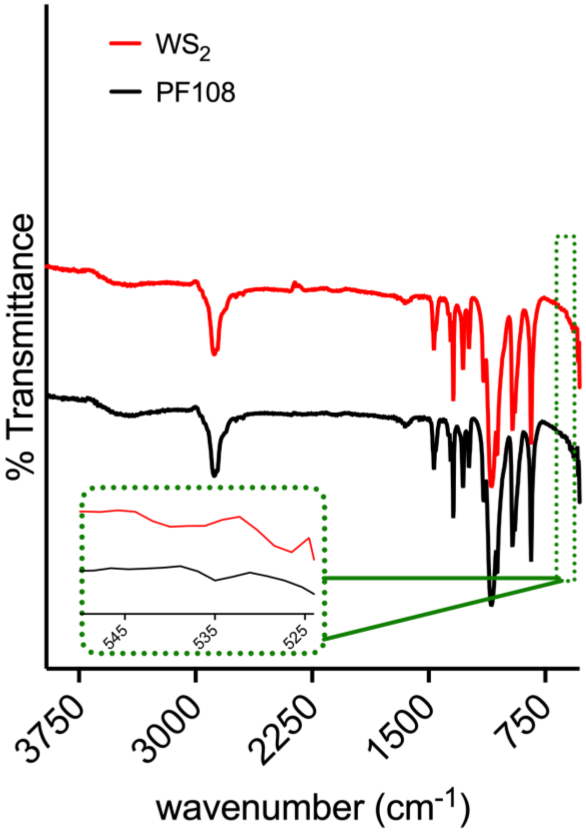

Figure S-5. FTIR spectra.The spectra for suspended WS_2 nanosheets is shown with red line. The spectra for PF-108, the surfactant used to suspend the WS_2 nanosheets, is displayed with a black line. The green dotted line box shows a zoomed in section of the FTIR spectra with a characteristic band at 526 nm for S-S bonds in the nanosheets.

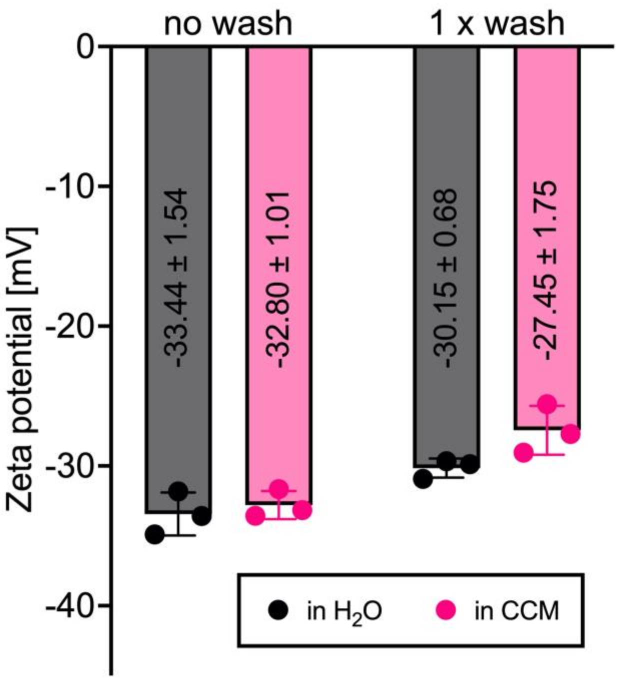

Figure S-6. ζ-potential of WS_2 nanosheets. The nanosheets were diluted to 30 µg/mL in water or cell culture media, incubated for an hour, and collected (16,000 × g; 20 mins). The nanosheets were either directly resuspended (no wash) or washed 1 × with H_2O then resuspended in DI H_2O with 0.1 mM NaCl (1 × wash) for zeta potential measurements. Bars represent the average ± SD (n=3).

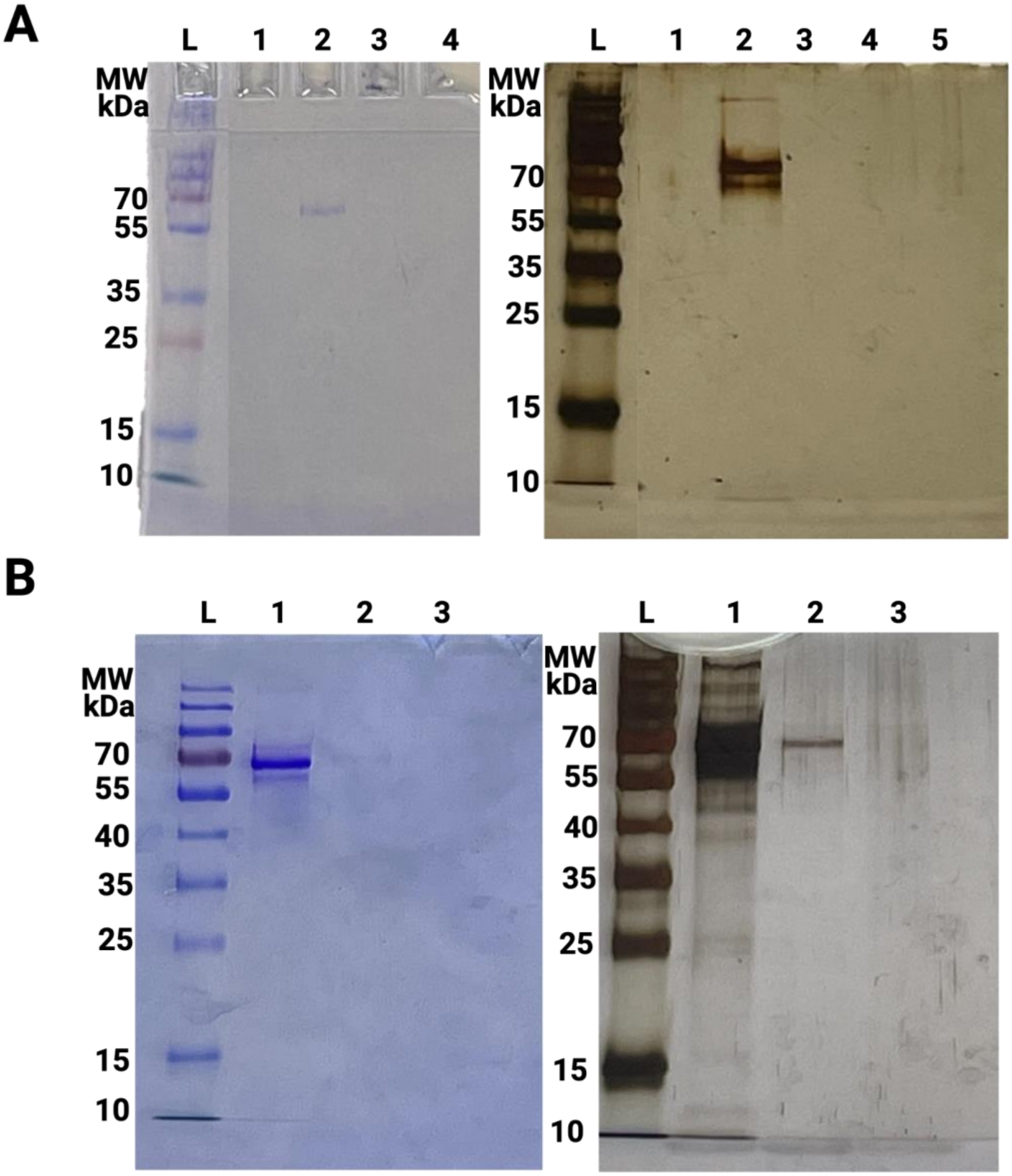

Figure S-7. SDS-PAGE confirms minimal protein adsorption on WS_2 isolated from CCM.L: molecular ladder. For each gel, the WS_2 concentration is 50 µg/mL. **A)** Lane 1: WS_2 diluted in H_2O without incubation in CCM. Lane 2: WS_2 were incubated in CCM for 1 h, pelleted (16,000 × g; 20 mins) and not washed. Lane 3: WS_2 were washed 1 × with 1× PBS. Lane 4: WS_2 nanosheets were washed twice. To determine if the surfactant (PF108) was preventing protein corona formation, the nanosheets were concentrated, following a protocol[2], to reduce dispersant levels. The gels in panel **B)** show increased protein adsorption following nanosheet concentration however, after washing the material, proteins were desorbed and removed. Lane 1: Concentrated WS_2 were incubated in CCM, pelleted (16,000 × g; 20 mins) and not washed. Lane 2: WS_2 were washed 1× with 1× PBS. Lane 3: WS_2 nanosheets were washed twice.

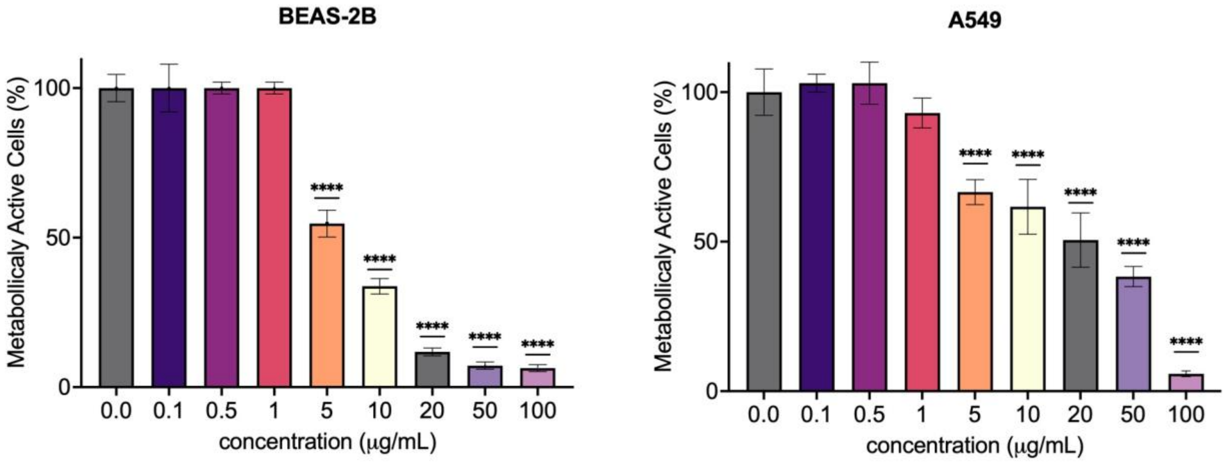

Figure S-8. Metabolically active cells following WS_2 exposure measured with CCK8. Cells were exposed for 24 h to 0 – 100 µg/mL WS2.The bars represent the mean ± SD (n=3). Cells treated with the WS_2 nanosheets are compared to control cells (0 µg/mL) and analyzed by 1-way ANOVA with Tukey correction. ****: $p < 0.0001$.

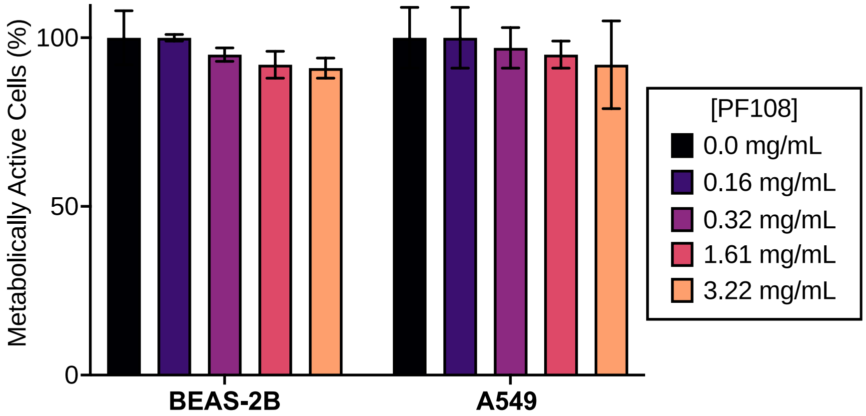

Figure S-9. Metabolically active cells following 24 h exposure to PF108.he PF108 concentrations (0-3.22 mg/mL) correspond to the approximate amount of PF108 cells were exposed to when they were treated with 0, 5, 10, 50, and 100 µg/mL WS_2, respectively. Metabolically efficiency was measured with CCK8. Bars represent mean ± SD (n=3).

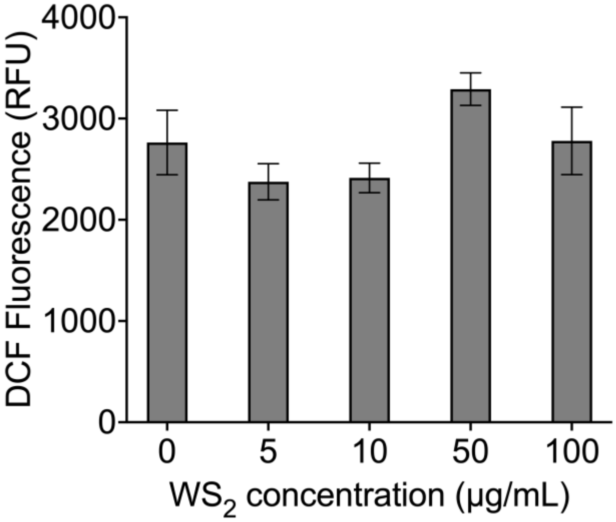

Figure S-10. WS_2 nanosheets, without H_2O_2, do not induce ROS in an abiotic system.The bars represent the mean ± SD (n=3).

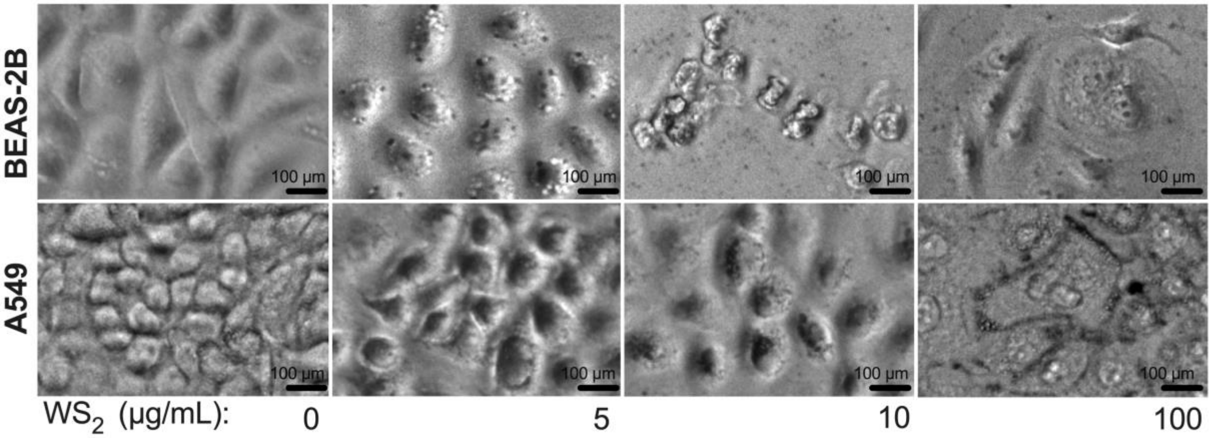

Figure S-11. Concentration-dependent cell morphological changes induced by WS_2. Scale bars: 100 μm.

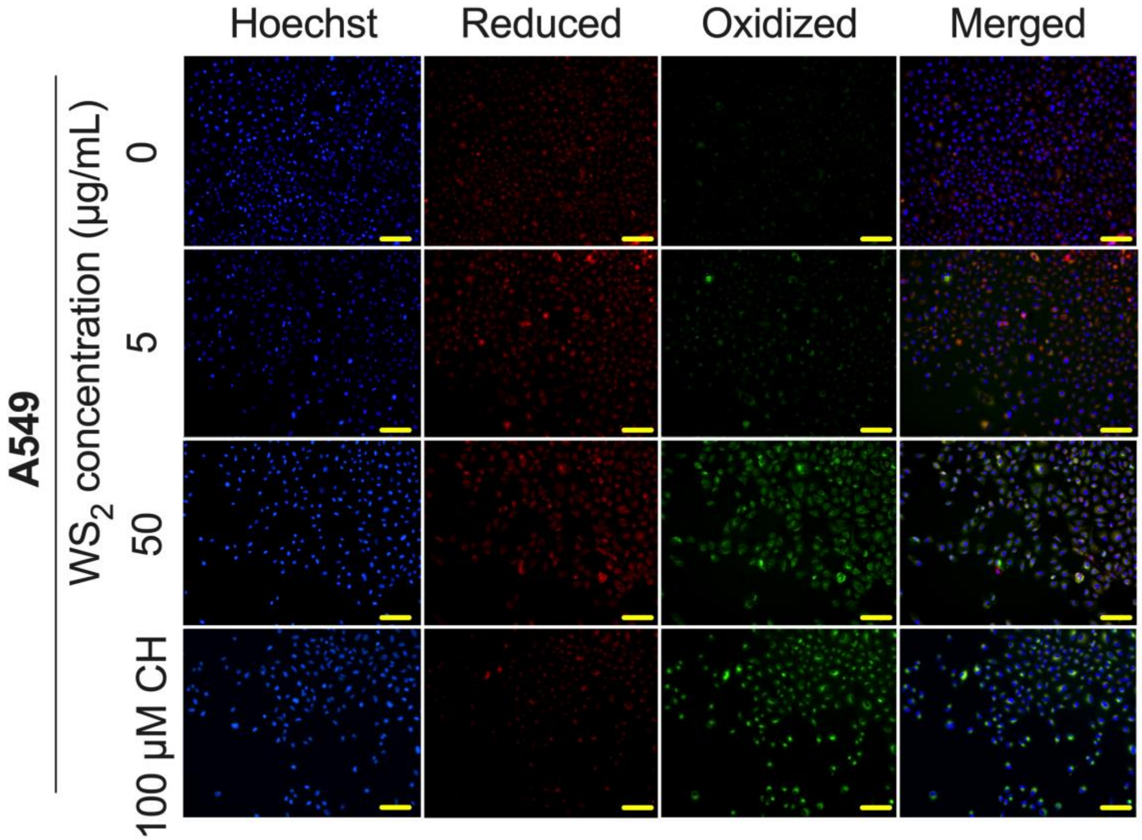

Figure S-12. Fluorescent images of peroxidation in A549 treated with WS_2. Scale bar: 100 µm.

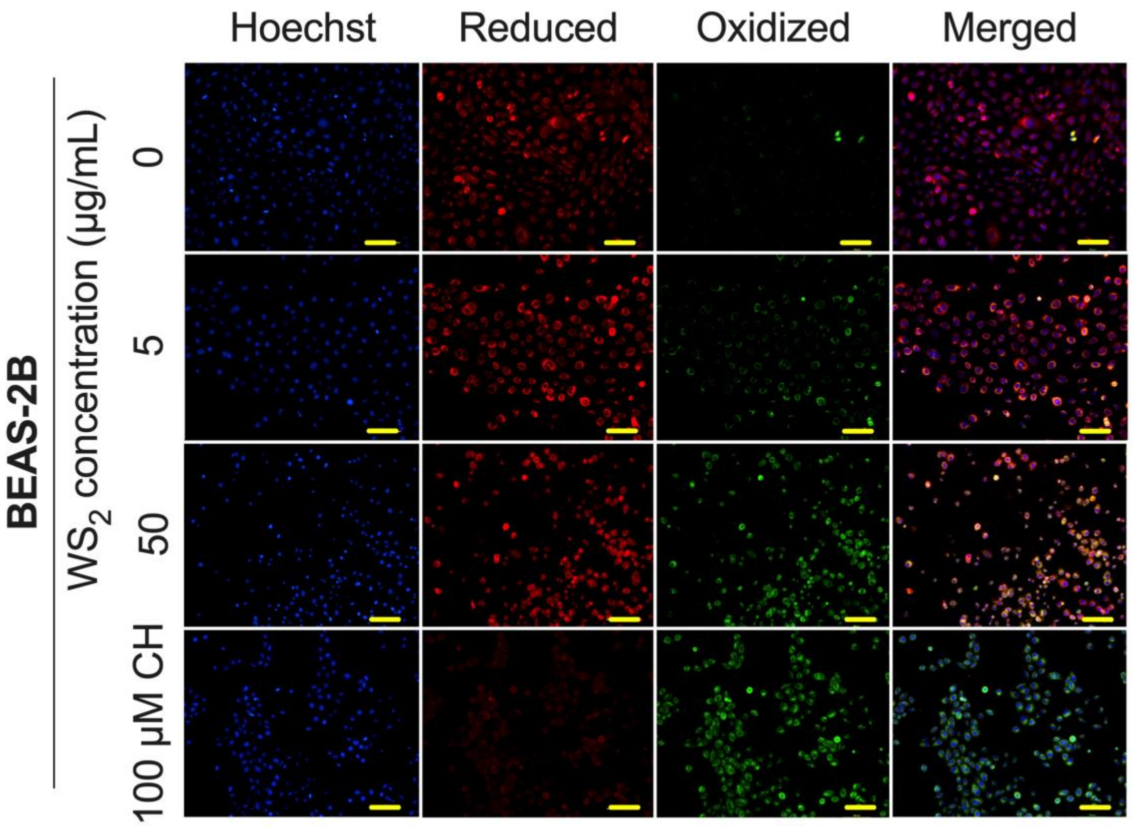

Figure S-13. Fluorescent images of peroxidation in BEAS-2B treated with WS_2. Scale bar: 100 µm.

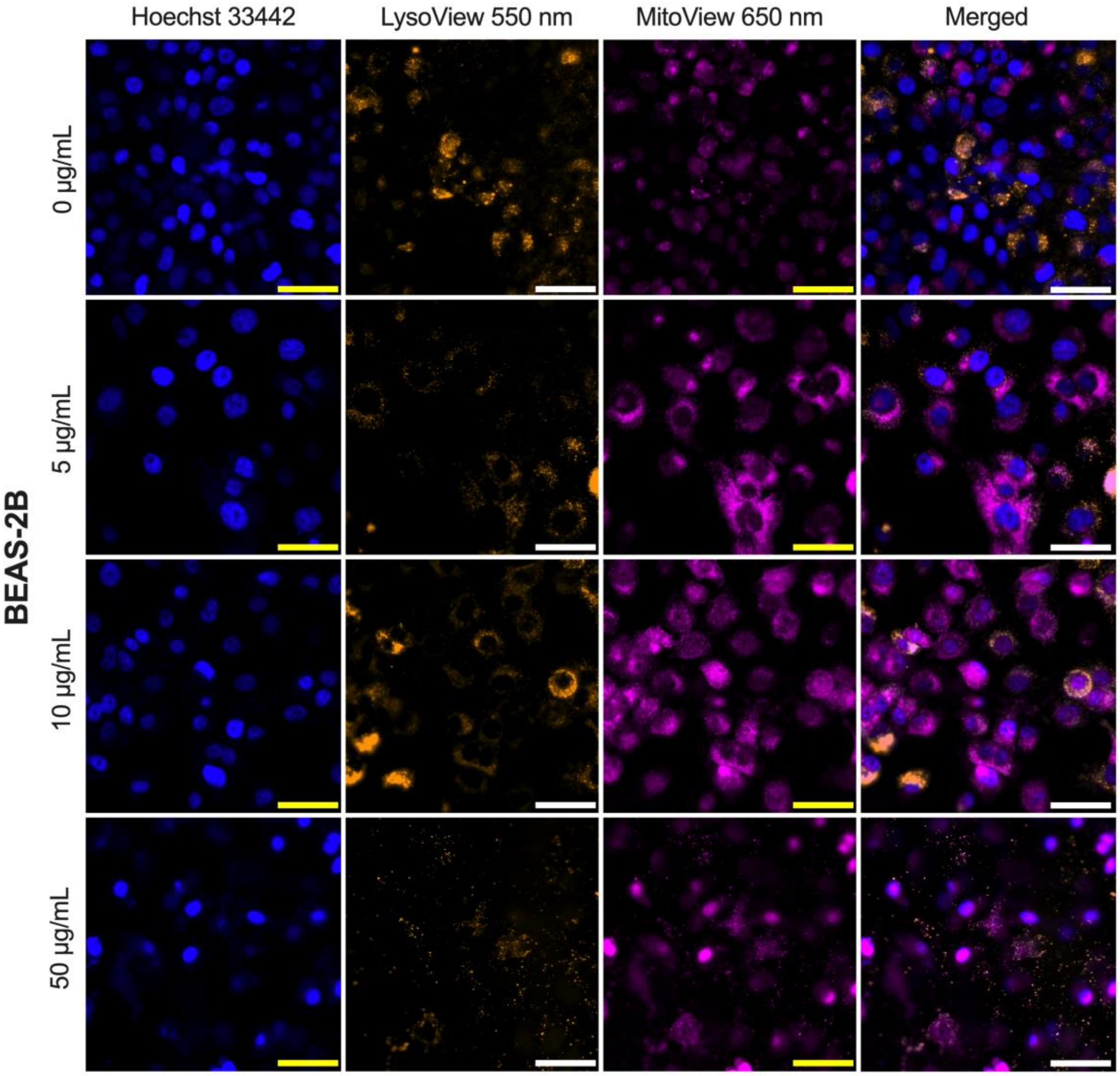

Figure S-14. WS_2 impact on BEAS-2B lysosomes. Lysosome, mitochondria and nuclei were stained with LysoView 550, MitoView 650 and Hoechst 33442 dyes following 24 h exposure to 0, 5, 10, and 50 μg/mL WS_2 nanosheets. The column furthest to the right reflects the merged images. Scale bars: 50 μm.

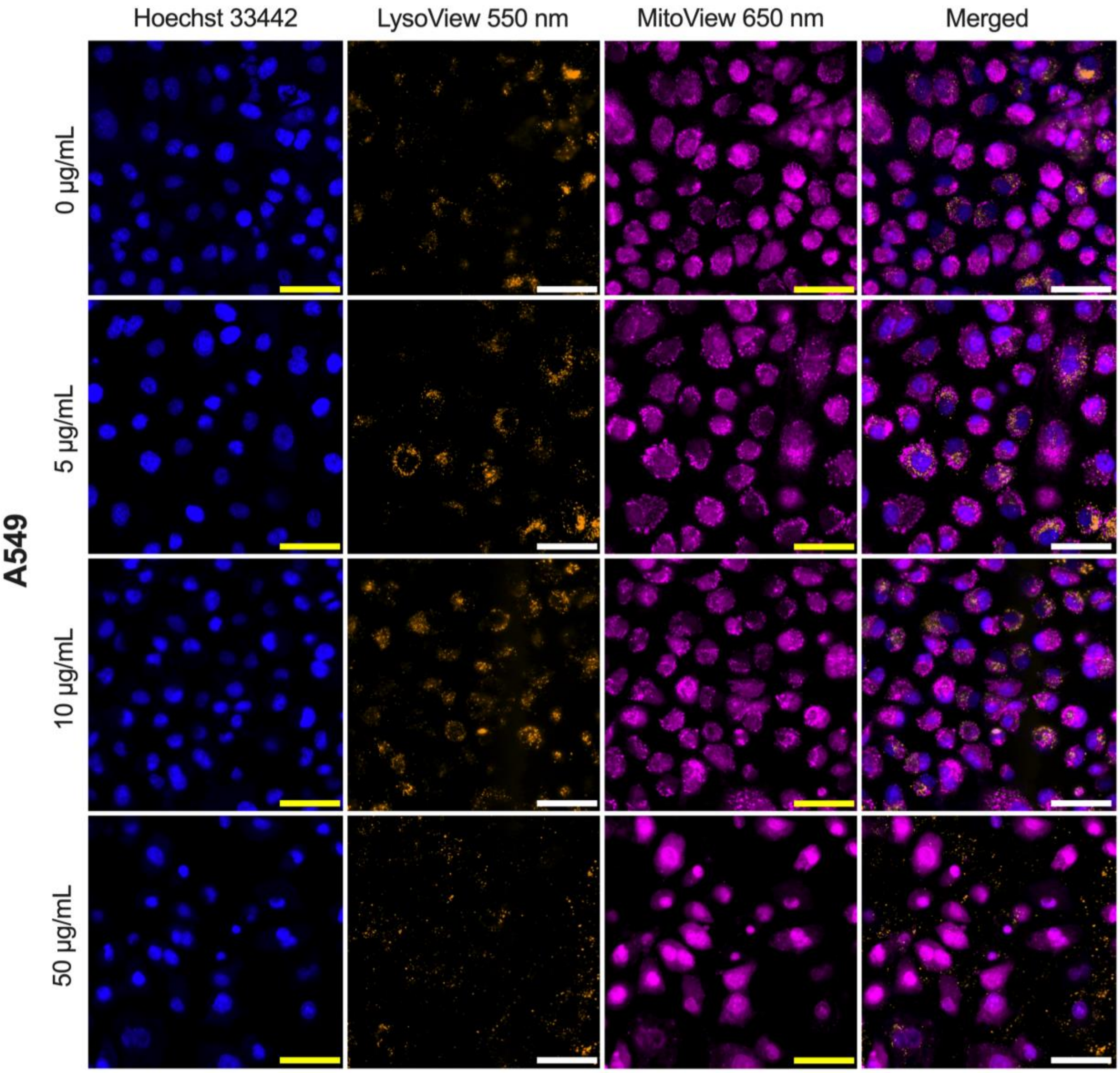

Figure S-15. WS_2 impact on A549 lysosomes.Lysosome, mitochondria and nuclei were stained with LysoView 550, MitoView 650 and Hoechst 33442 dyes following 24 h exposure to 0, 5, 10, and 50 µg/mL WS_2 nanosheets. The column furthest to the right reflects the merged images. Scale bars: 50 µm.

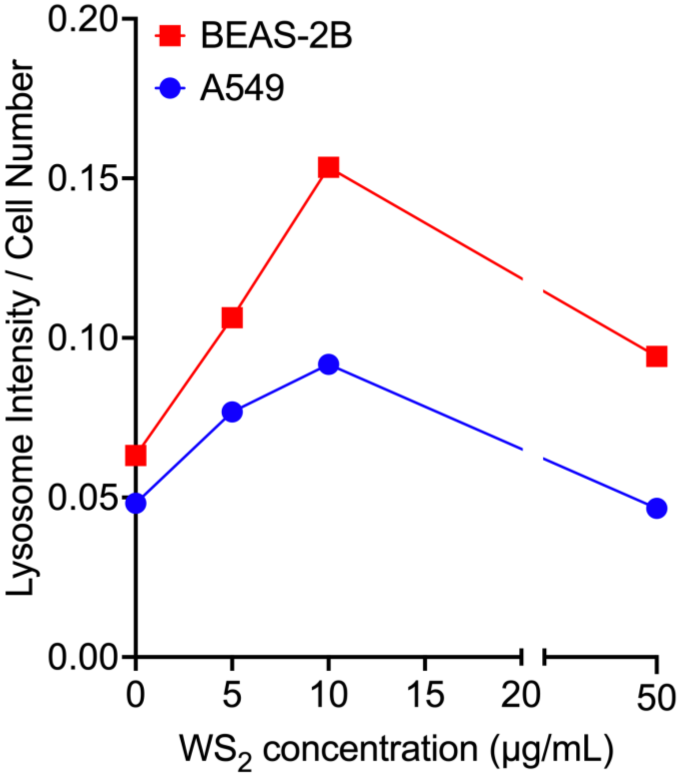

Figure S-16. Lysosome signal intensity following WS_2 exposure.The signal from stained lysosomes was quantified using ImageJ and these values was normalized to the counted cell numbers in the fluorescence images from Figs. S-14 and S-15.

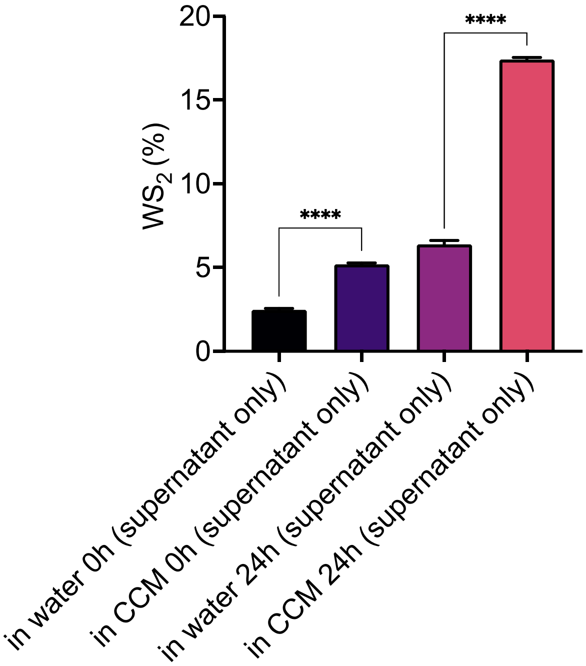

Figure S-17. Dissolved WS_2 nanosheets measured with ICP-OES.ICP-OES was used to measure the amount of dissolved WS_2 nanosheets in the supernatants of samples prepared in water or cell culture media (CCM). The values were normalized to the average value of the dissolved control (5 µg/mL digested with aqua regia). Bars represent the mean ± SD. *** $p < 0.001$, **** $p < 0.0001$, 1-way ANOVA with Tukey corrections.

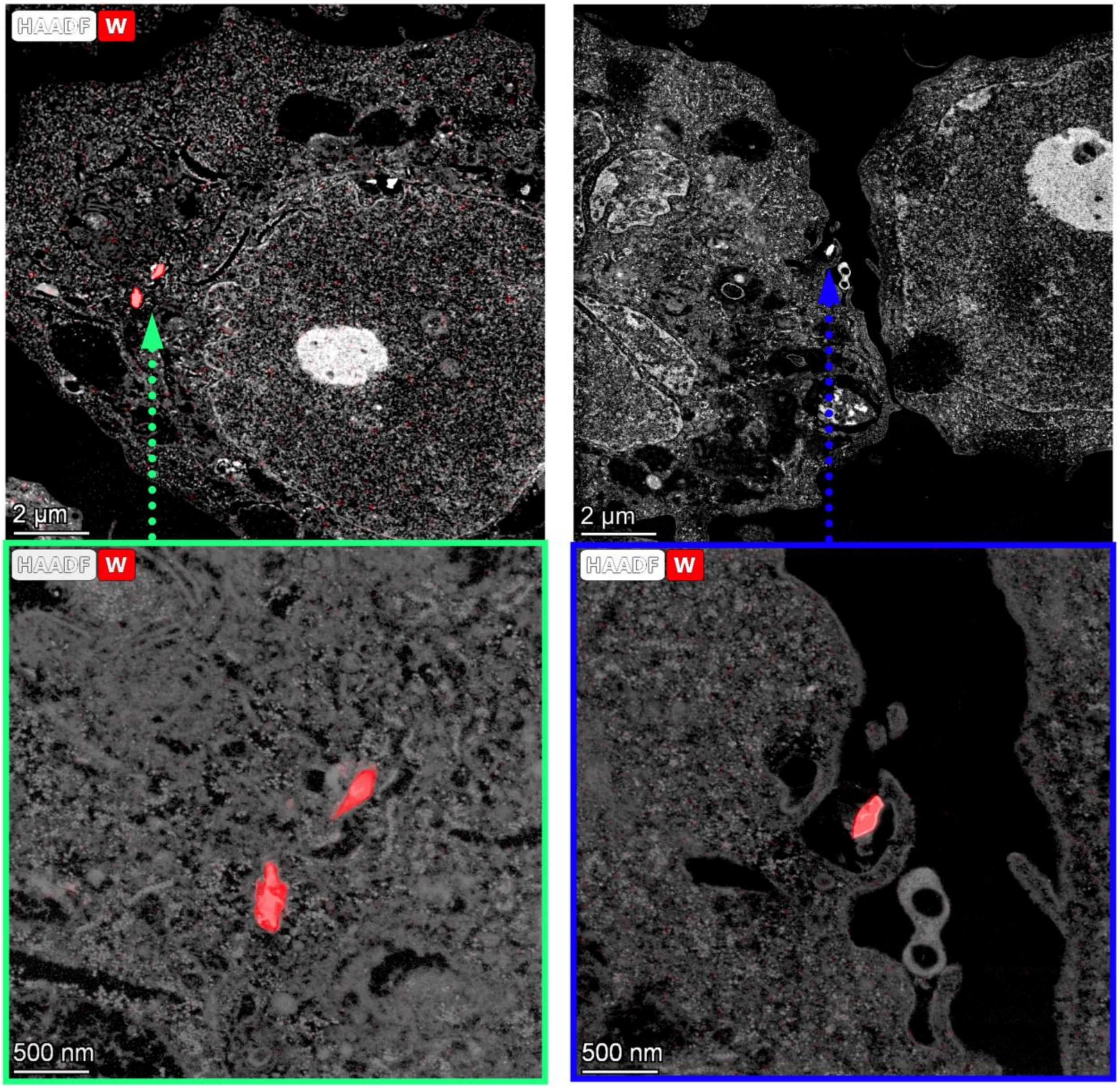

Figure S-18. Internalized WS_2 nanosheets in BEAS-2B cells revealed by TEM with EDS.Scale bars: 2 µm and 500 nm.

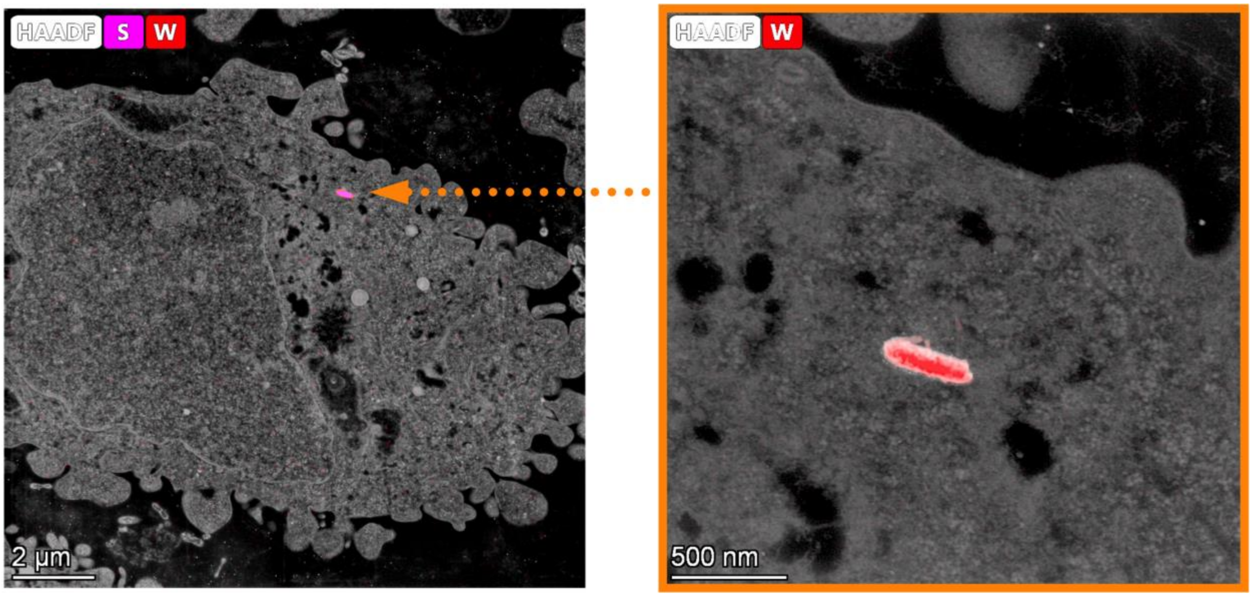

Figure S-19. Internalized WS_2 nanosheets in A549 cells revealed by TEM with EDS.Scale bars: 2 µm and 500 nm.

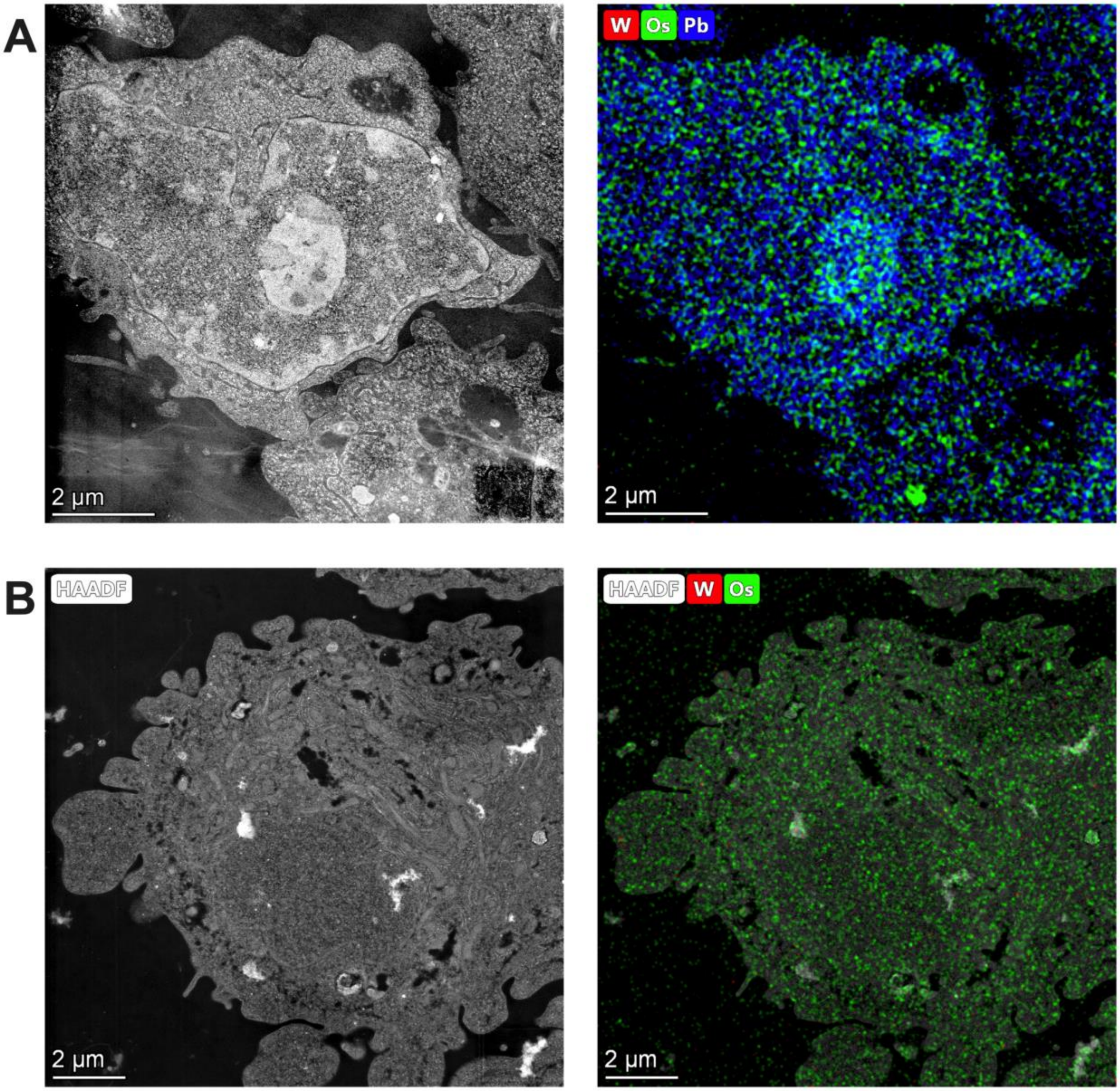

Figure S-20. TEM of control cells.**A)** HAADF and EDS images of a control BEAS-2B cell. **B)** HAADF and EDS images of a control A549 cell. Elemental mapping confirms the absence of elemental tungsten inside untreated control cells. Scale bars: 2 µm.

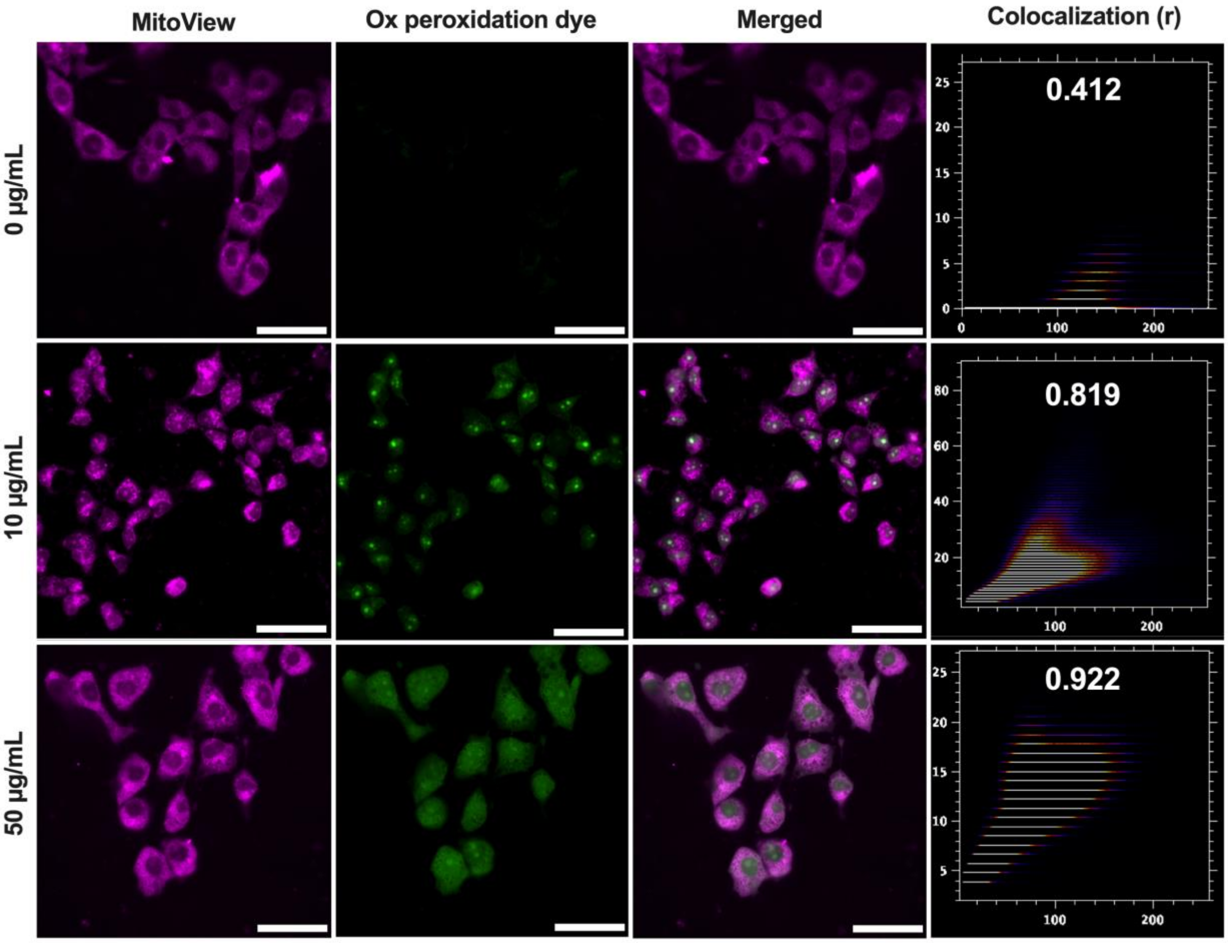

Figure S-21. Colocalization of mitochondria with membrane peroxidation in BEAS-2B.Scale bars: 100 µm.

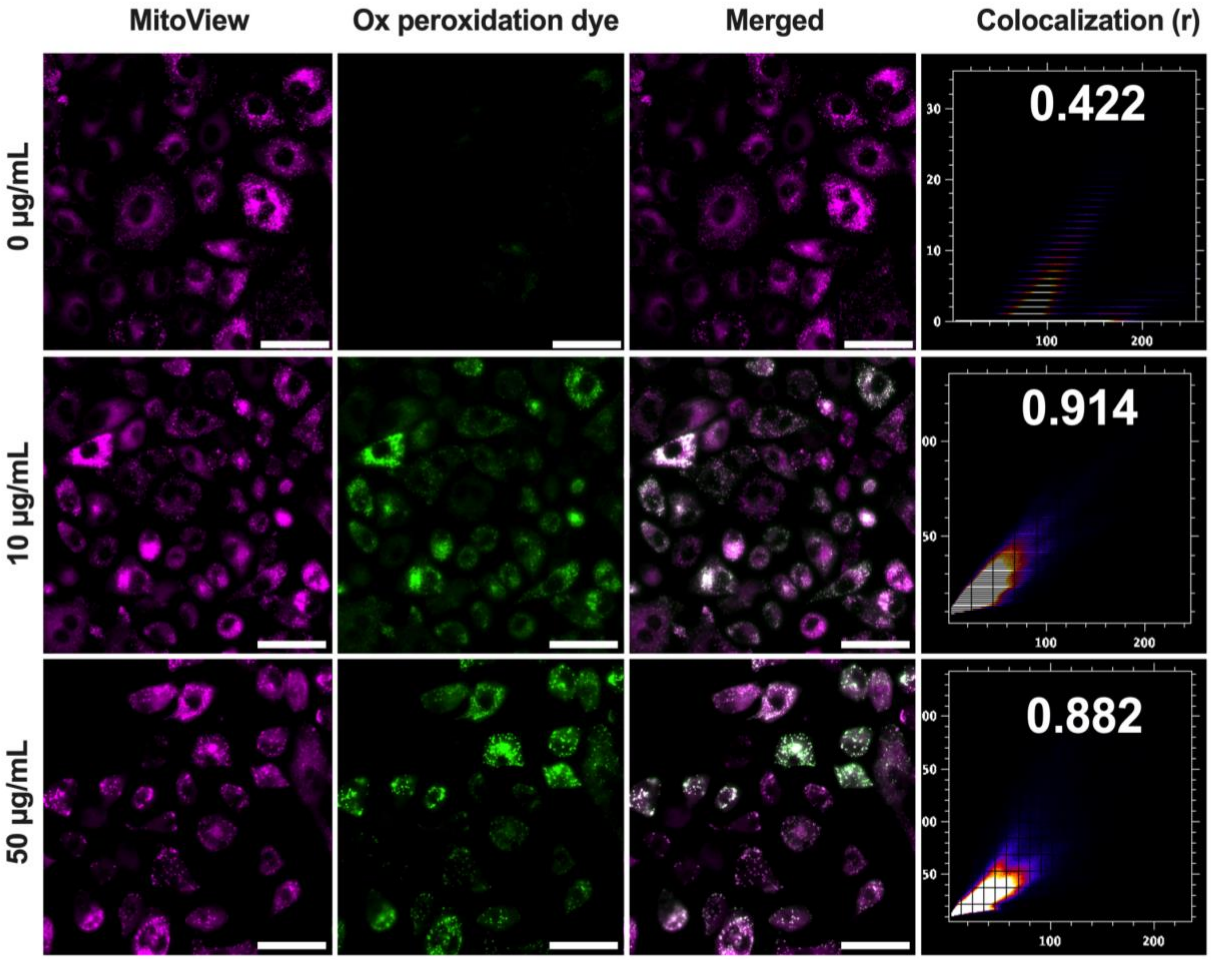

Figure S-22. Colocalization of mitochondria with membrane peroxidation in A549.Scale bars: 100 µm.

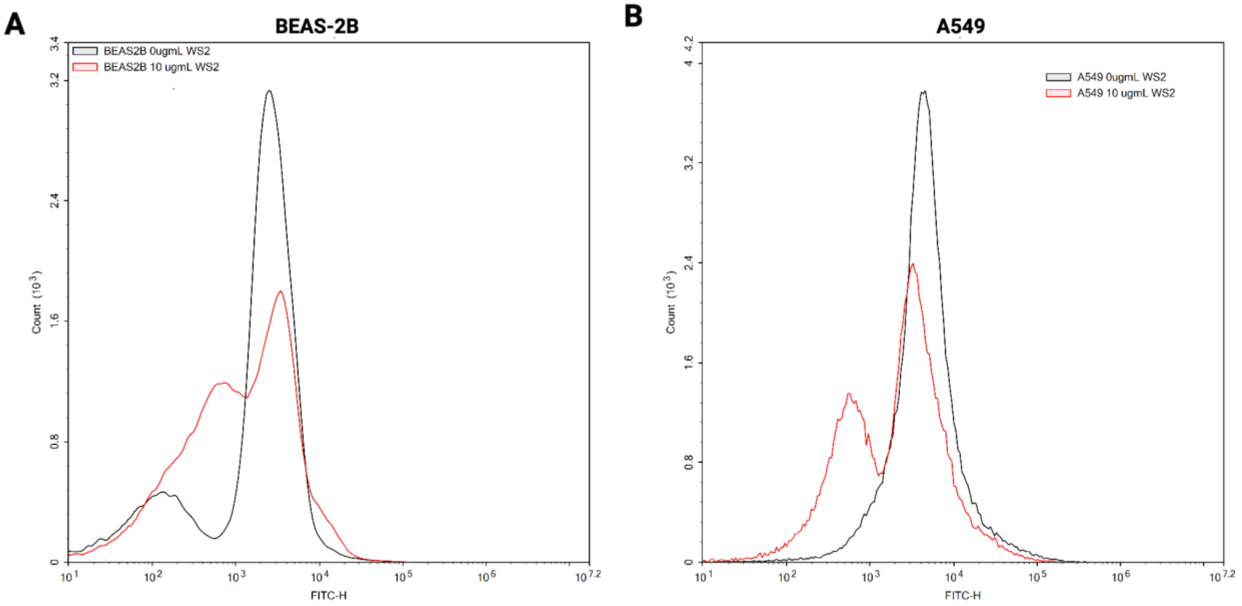

Figure S-23. Mitochondrial membrane potential ($\Delta\Psi_m$) following exposure to WS_2.Unexposed **A)** BEAS-2B and **B)** A549 cells (black trace), show minimal changes to $\Delta\Psi_m$. Treatment with 10 µg/mL WS_2 (red trace) resulted in $\Delta\Psi_m$ changes.

A **Real-time exposure**

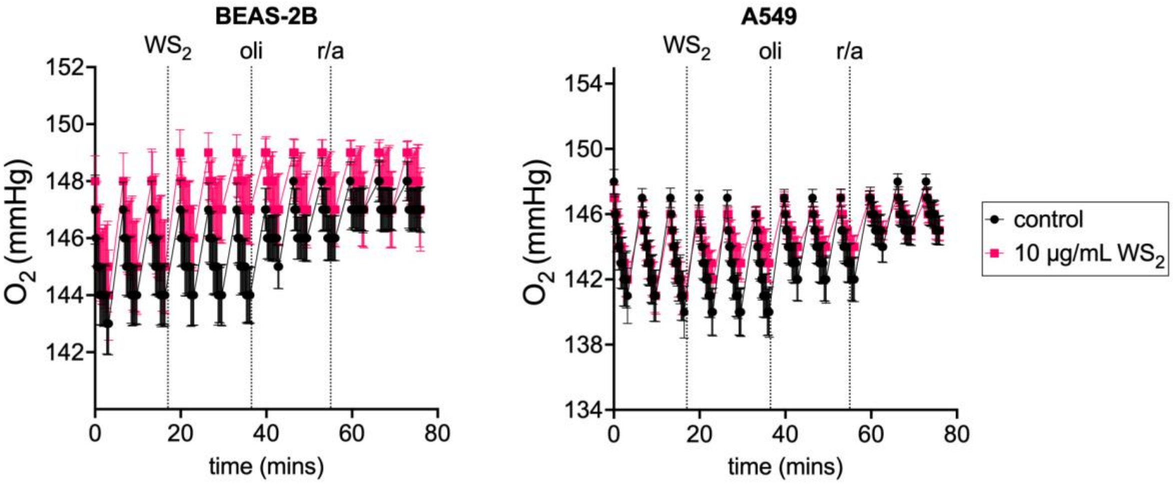

B **Pre-exposure**

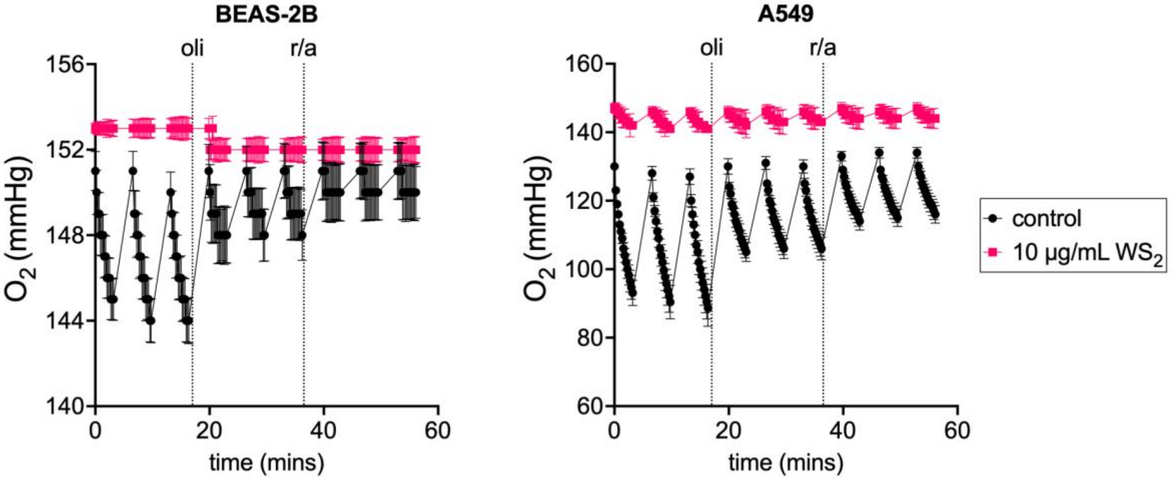

Figure S-24. Dysregulation of mitochondria function induced by 10 µg/mL WS_2. Oxygen tension profiles of BEAS-2B and A549 cells exposed **A)** in real-time, and **B)** pretreated for 24 h, with 10 µg/mL WS_2. Oligomycin (oli) and a mixture of rotenone and antimycin A (r/a) were injected at specific timepoints (to a final concentration of 1.5 µM and 0.5 µM, respectively) to assess ATP production by glycolysis and oxidative phosphorylation. Each point represents an average measurement ± SD (n=3).

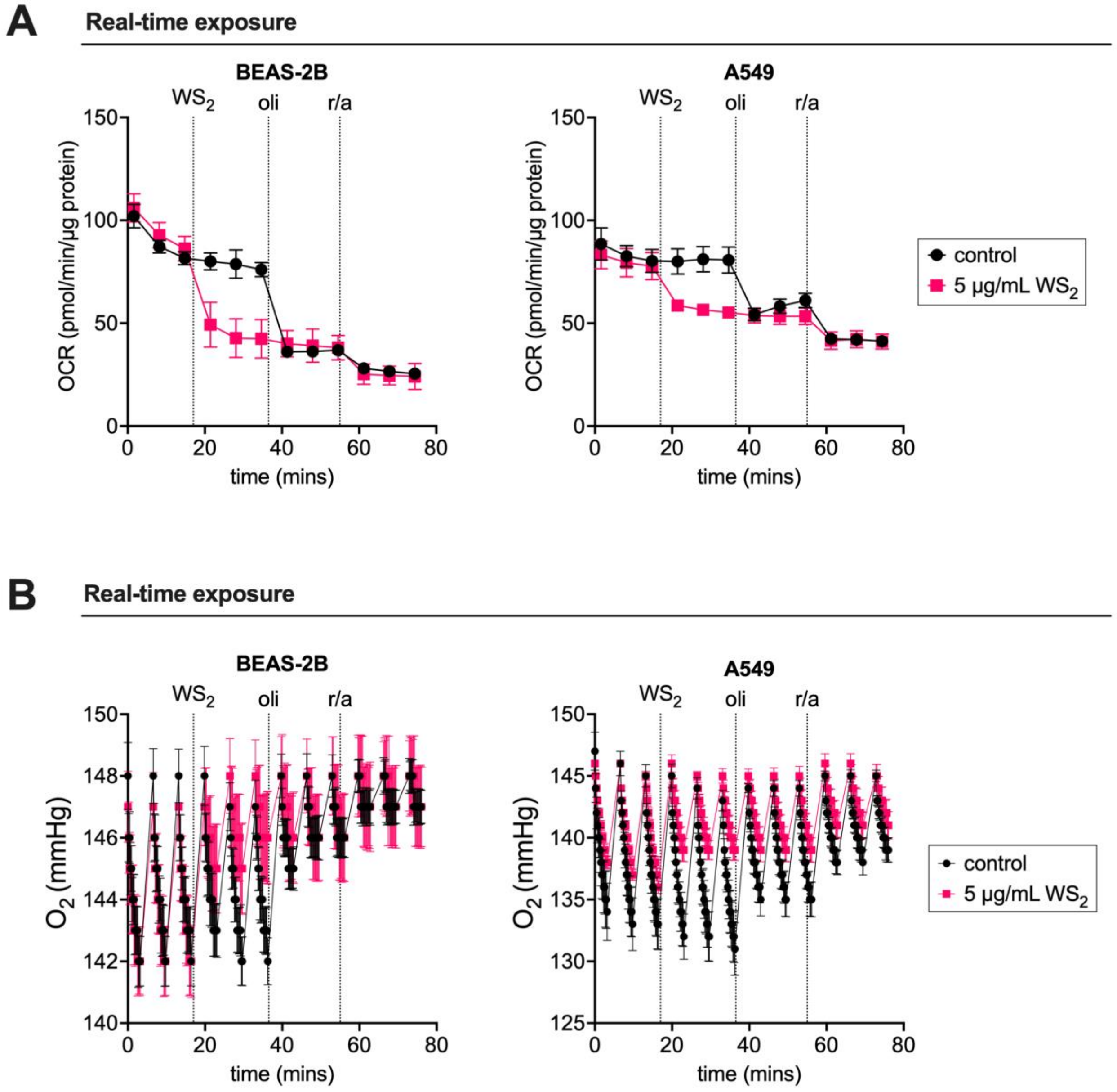

Figure S-25. Dysregulation of mitochondria function induced by 5 µg/mL WS_2. **A)** OCR and **B)** oxygen tension profiles of BEAS-2B and A549 cells exposed in real-time to 5 µg/mL WS_2. Oligomycin (oli) and a mixture of rotenone and antimycin A (r/a) were injected at specific timepoints (to a final concentration of 1.5 µM and 0.5 µM, respectively) to assess ATP production by glycolysis and oxidative phosphorylation. Each point represents an average measurement ± SD (n=3).

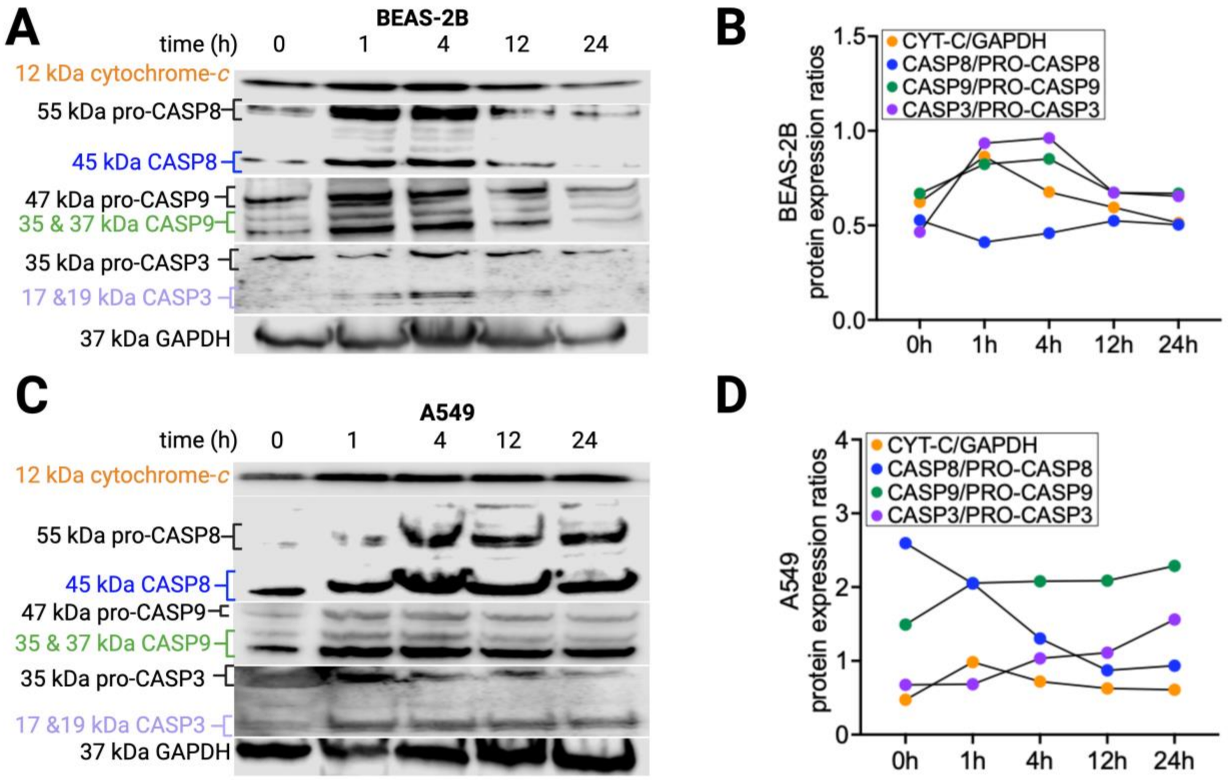

Figure S-26. Immunoblots for apoptosis related protein expression in cells.Immunoblots of cytochrome-*c*, GAPDH (loading control), as well as activated and inactivated caspase proteins from **A)** BEAS-2B lysates and **C)** A549 lysates. Protein expression in **B)** BEAS-2B and **D)** A549 quantified from immunoblots with ImageJ.

References

(1) Bazina, L.; Bitounis, D.; Cao, X.; Deloid, G. M.; Parviz, D.; Strano, M. S.; Lin, H. Y. G.; Bell, D. C.; Thrall, B. D.; Demokritou, P. Biotransformations and Cytotoxicity of Graphene and Inorganic Two-Dimensional Nanomaterials Using Simulated Digestions Coupled with a Triculture: In Vitro Model of the Human Gastrointestinal Epithelium. *Environ. Sci. Nano* **2021**, *8* (11), 3233–3249. https://doi.org/10.1039/d1en00594d.

(2) Coreas, R.; Castillo, C.; Li, Z.; Yan, D.; Gao, Z.; Chen, J.; Bitounis, D.; Parviz, D.; Strano, M. S.; Demokritou, P.; Zhong, W. Biological Impacts of Reduced Graphene Oxide Affected by Protein Corona Formation. *Chem. Res. Toxicol.* **2022**, *35* (7), 1244–1256. https://doi.org/10.1021/acs.chemrestox.2c00042.